1-1-2014

Photonic Crystal-Based Flow Cytometry

Justin William Stewart
University of South Florida, stewartjw91@gmail.com

Photonic Crystal-based Flow Cytometry

by

Justin W. Stewart

A thesis submitted in partial fulfillment
of the requirements for the degree of
Master of Science in Chemical Engineering
Department of Chemical and Biomedical Engineering
College of Engineering
University of South Florida

Major Professor: Anna Pyayt, Ph.D.
Robert Frisina Jr., Ph.D.
John Kuhn, Ph.D.

Date of Approval:
October 29, 2014

Keywords: Biomedical Optics, Single Cell Detection, Lab on Chip, Modeling

DEDICATION

I would like to dedicate this thesis to my parents, James and Donna Stewart, for always taking time to assist me in my times of need, and for helping me become the man I am today. As a child, you saw within me an inquisitive spirit, curious about the world and eager to understand how and why things work. Together, you worked to make sure that these traits would always stay with me, and set me along the path of future scientific endeavors. And for this I am eternally grateful.

TABLE OF CONTENTS

LIST OF FIGURES

ABSTRACT

Photonic crystals serve as powerful building blocks for the development of lab-on-chip devices. Currently they are used for a wide range of miniaturized optical components such as extremely compact waveguides to refractive-index based optical sensors. Here we propose a new technique for analyzing and characterizing cells through the design of a micro-flow cytometer using photonic crystals. While lab scale flow cytometers have been critical to many developments in cellular biology they are not portable, difficult to use and relatively expensive. By making a miniature sensor capable of replicating the same functionality as the large scale units with photonic crystals, we hope to produce a device that can be easily integrated into a lab-on-chip and inexpensively mass produced for use outside of the lab.

Using specialized FDTD software, the proposed technique has been studied, and multiple important flow cytometry functions have been established. As individual cells flow near the crystal surface, transmission of light through the photonic crystal is influenced accordingly. By analyzing the resulting changes in transmission, information such as cell counting and shape characterization have been demonstrated. Furthermore, correlations for simultaneously determining the size and refractive indices of cells has been shown by applying the statistical concepts of central moments.

CHAPTER 1

INTRODUCTION

1.1 Note to Reader

Portions of this chapter have been adapted from work that has been previously published in *Optics Express,* 2014, 22, 12853-12860, and has been reproduced with permission from the Optical Society of America.

1.2 Motivation

Analytical methods for studying individual cells with high throughput have been critical for molecular biology, immunology and pathology. In addition, advancements in high throughput cell screening have greatly assisted in the discovery of new drugs. Among available techniques, flow cytometry has become the most widely used method for analyzing and characterizing cells [1]. Traditional flow cytometry units are complex systems which employ multiple lasers and sophisticated optical detectors designed primarily for cell counting, shape characterization, and multi-colored fluorescence analysis [2]. Despite having many benefits, these systems have significant limitations due to their large size, high prices and complex operation [3].

Today, the rising need for 'Point-of-Care' devices has led to an increased demand for more portable, and lower cost flow cytometers. While, benchtop units are still the smallest among commercially available flow cytometers, and they are heavy and not readily portable [3]. Ongoing research in miniaturizing flow cytometers into handheld devices has made significant progress

over the past few years. Nonetheless, smaller devices have had to sacrifice many capabilities, including detection on multiple wavelengths [4]. Another promising method relies on digital processing of diffraction patterns of different cell types [5]. However, these diffraction pattern techniques are not performed using flowing fluids, therefore continuous cell differentiation cannot be achieved [5].

1.3 Background

1.3.1 Micro Flow Cytometry

Advances in MEMS and microfluidics has provided an opportunity to reproduce the functionality of large scale flow cytometry units with high cell throughput, at much smaller scale. The proposed micro-flow cytometers often incorporate some method of spatial cell focusing in conjunction with optical, magnetic or electrical detection components, into a single device that can easily fit onto a chip [6]. Nevertheless, micro-flow cytometers have experienced difficulty in providing functions analogous to traditional flow cytometers due to either more complex detection methods or lower resolution optical detectors. Specifically, devices relying on magnetic detection suffer from increased complexity in sample preparation, as cells are not inherently magnetic. As a result, cells must be labeled with magnetic nanoparticles, before they can be detected [7-9]. Additionally, while demonstrating great promise in continuously counting cells, magnetic and electric-based micro-flow cytometers were unable to perform certain functions such as fluorescent studies for cellular expression. On the other hand, optics-based micro-flow cytometers struggle with low resolution. At the microscale, light diffracts at wide angles, and as a result there are significant losses between light sources and detectors. In order to overcome diffraction limitations, waveguides and optical detectors are often very large, to the point that these components are

generally several cell diameters in width [10, 11]. Due to this, optical detection in micro-flow cytometry often experiences difficulty resolving individual cells within close proximity of each other due to the optical components high field of view [10, 11]. One potential method to overcome the pitfalls that have plagued the field of micro-flow cytometry is to use photonic crystals.

1.3.2 Photonic Crystals

Over the last 50 years, interest in new devices created with photonic crystals has grown greatly, due in part to their capability of manipulating light on extremely small scales. Photonic crystals are structures containing periodic variations of refractive index often realized as micro-fabricated pores, slits or other types of "defects." As light passes through these fluctuations of refractive index, reflection occurs at the many interfaces within the crystal. As a result, interference between waves that are simultaneously reflected, transmitting and scattered within the crystalline structure produces unique spectral features such as photonic band gaps (i.e. wavelengths where light is incapable of transmitting through the structure) and spectral regions of high transmission. By periodically alternating the refractive index of the structure, taking into consideration the wavelengths of light, as well as the size, periodicity and overall number of defects found within the photonic crystal, distinct transmission spectra can be engineered.

The types of photonic crystals are generally classified by order of dimensions for which the periodic defect is repeated throughout the bulk material. These are namely one (1-D), two (2-D) and three dimensional (3-D) photonic crystals (PhCs).

Traditionally, PhCs have found many applications depending on the overall structure of the crystal. 1-D PhCs are mostly being used in the field of thin film optics to create coatings for lenses and mirrors which are highly wavelength selective, as well as for the production of color shifting inks that appear different hues depending on the angle at which they are viewed [12]. 2-D

PhCs are commonly used for the manufacturing of highly lossless photonic crystal fibers (PCFs). These PCFs are capable of confining light within a core surrounded by PhCs exhibiting a photonic band gap for the operating wavelength, as well as control chromatic dispersion while filtering light of undesired wavelengths [13]. Meanwhile 3-D PhCs, are not as widely available, though they have already demonstrated potential in the field of optically integrated circuits [14]. Additionally, PhCs are being applied to novel devices for refractive index based sensing [15] as an alternative to other refractive index-based sensing methods [16-18]. Yet, PhCs remain an area of with a lot of ongoing research as they allow direct manipulation and control of light at the micron scale, and can be easily integrated into lab-on-chip devices, making the miniaturization of many apparatuses and sensing equipment possible.

1.4 Thesis Organization

In this thesis, we propose a new method of performing micro-flow cytometry using the transmission spectra of a photonic crystal (PhC) to analyze multiple parameters of cells simultaneously, while traditionally PhCs have been used for refractive index-based sensing [15, 19]. Based on FDTD simulations, we demonstrate that by using more sophisticated spectrum analysis it is possible to design a PhC micro-flow cytometer capable of achieving functionality similar to traditional flow cytometry units, however at a significantly smaller scale and potentially lower cost.

The thesis is composed of eight chapters. In chapter one, introductions to flow cytometry as well as photonic crystals are given, including the motivation for designing the device. In chapter two, a literature review regarding various methods for focusing cells in micro-flow cytometry is provided. Chapter three is a summary of the relevant partial differential equations used in modeling

the photonic crystal device, as well as an overview of the numerical method used and the assumptions made to simplify the equations. In chapter four we describe the modeling of the device and how it would operate in theory, while also giving the parameters used in the simulations. Chapter five provides a preliminary set of results, demonstrating how spectral information from a PhC is calculated, as well as a few tests of the PhCs behavior. In Chapter six, results of the micro-flow cytometry simulations are presented, as well as an analysis and discussion of the results. In Chapter seven we provide further considerations and recommendations for the project, as well as a vision for where we hope the device might be applied, and chapter eight gives the conclusions and final thoughts.

CHAPTER 2

CELL FOCUSING TECHNIQUES

2.1 Introduction

In order to perform flow cytometry, cells must first be aligned into a stream of individual cells, after which they are permitted to pass through a detection system (optical, electrical, magnetic, etc.) Otherwise, randomized cell flow through a cytometry device would provide arbitrary results with no merit or usefulness. As the field of microfluidics has become increasingly popular, concepts and techniques for ordering and focusing cells within lab-on-chip devices have rapidly emerged, while new research into micromanipulation of cell flow continues to grow.

Among the multiple cell manipulation methods available, such as: inertial focusing, hydrophoretic focusing, focusing using grooved micro-channels, and focusing with standing acoustic waves, the majority of techniques organize cells in a single stream at the center of the microfluidic channel [20-23]. However, for situations such as PhC micro-flow cytometry, where the detector is located at the surface of the micro-channel, cells are required to flow in close proximity to the detector in order to maximize sensitivity. There are several methods available that can create uniform cell streams at or near the surface of a microfluidic channel. These techniques may easily be implemented into the device, making it possible to perform PhC flow cytometry with the configuration proposed in later chapters.

2.2 Passive Cell Ordering Using Lateral Forces

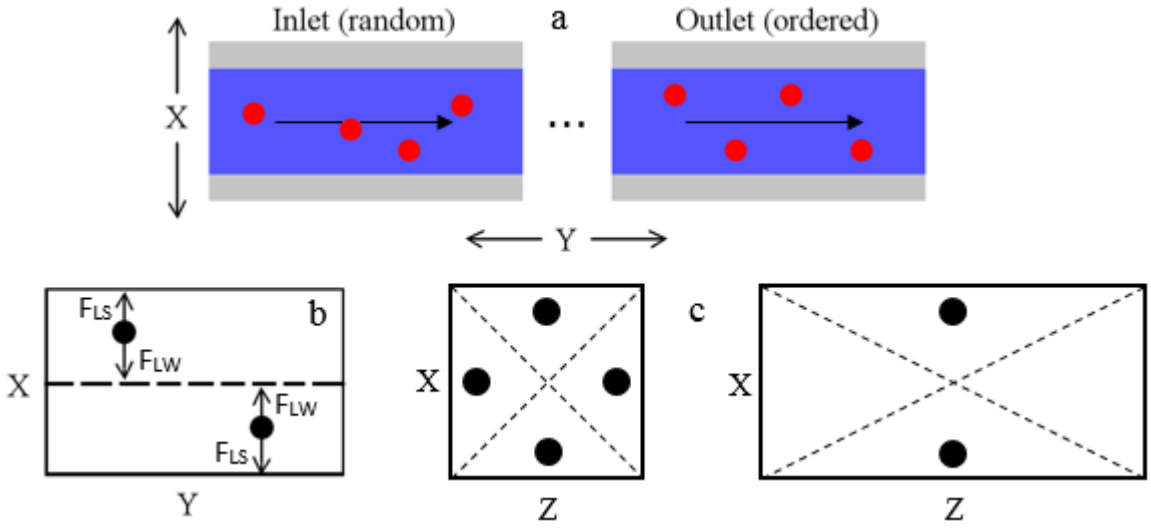

Figure 1. Demonstration of cell ordering through lateral forces. (a) Cells injected at the inlet of a microfluidic channel are in random configuration, yet once they reach the outlet cells will be ordered. (b) Force diagram showing the lateral forces acting on cells within the channel. (c) Positions of cell streams (shown as dots) in the X-Z plane for square and rectangular channels. Flow is in the Y direction.

The first technique is a passive method for microfluidic cell focusing, and is the simplest to implement in a flow cytometry system. When cells are injected into a microfluidic channel in random orientation, they will naturally order into focused streams over time, as shown in Figure 1(a), when flow is laminar. At the small scales used in microfluidic systems, where hydraulic diameters (D_H) of micro-channels are on the order of nanometers to micrometers, the Reynolds number ($Re = \rho_f V D_H / \mu$), a ratio of the inertial forces to viscous forces within the fluidic system, is typically very small and exists well within the laminar regime (Re<2300).

Under laminar flow conditions, cells in a micro-channel are subjected to primarily two opposing lateral forces; wall effect lift (F_{LW}) and shear-gradient lift (F_{LS}) [10]. Due to the parabolic nature of laminar velocity profiles, cells are driven from the center of flow, and forced to move towards the closest wall on either side of the channel by the shear-gradient lift. Additionally, as

cells approach the walls, pressure between the cell and wall begins to increase, inducing wall effect lift upon the cell, pushing it towards the center of the channel. In Figure 1(b), a force diagram is provided, demonstrating the described effects. Once a sufficient distance (L_F) has passed, the cell will reach an equilibrium position (X_{EQ}) from the wall where the forces are balanced [24]. This is commonly known as the Segre-Silberberg effect, and the equilibrium positions for a rectangular channel may be approximated by the expression [24,25];

$$X_{eq} \cong X_C \pm 0.3X_H \quad \text{(eq.1)}$$

here X_C denotes the center of the microfluidic channel, and X_H is the total height of the channel. The critical channel length required to achieve lateral focusing (L_F) can be calculated using this equation:

$$L_F = \frac{\pi \mu X_H^2}{\rho_f V_m D_{cell}^2 f_L} \quad \text{(eq.2)}$$

where μ and ρ_f are the viscosity and density of the fluid surrounding the cell respectively, V_m is the maximum velocity within the channel, D_{cell} is the diameter of the cell, and f_L is the average lift coefficient, varying from 0.02 to 0.05 depending on the channel aspect ratio (height/width) [10]. When the channel aspect ratio is near one (i.e. the channel is square), cells focus into four distinct streams due to the fourfold symmetry of the channel. However, when the channels are rectangular, and aspect ratio decreases to 0.5 and lower, cells will only focus into two streams located along the top and base of the channels, as shown in Figure 1(c) by the black spots [10]. In addition, when the Reynolds number of the particle (Re_p) is on the order of 1, cells orient themselves in a staggered spacing, as seen in the outlet of Figure 1(a).

By using lateral forces it is easy to focus cells for micro-flow cytometry by simply placing the detector at a distance greater than L_F from the inlet of the channel. Studies using polystyrene

beads (diameter 9.9 µm) in a 16 µm thick channel, have shown that the particles can be focused to a distance of approximately 1.37 µm from the channel surface [10]. Given that the PhC is not aligned with the channel surface and is slightly raised, this would be sufficient to allow for cell detection. Although, due to the nature of the Segre-Silberberg effect, cells focus into two streams at both the top and base of the channel. As a result, only half of the cells in the sample would be within range for detection by the PhC.

2.3 Sheath-Free Cell Focusing With Geometry Induced Flows

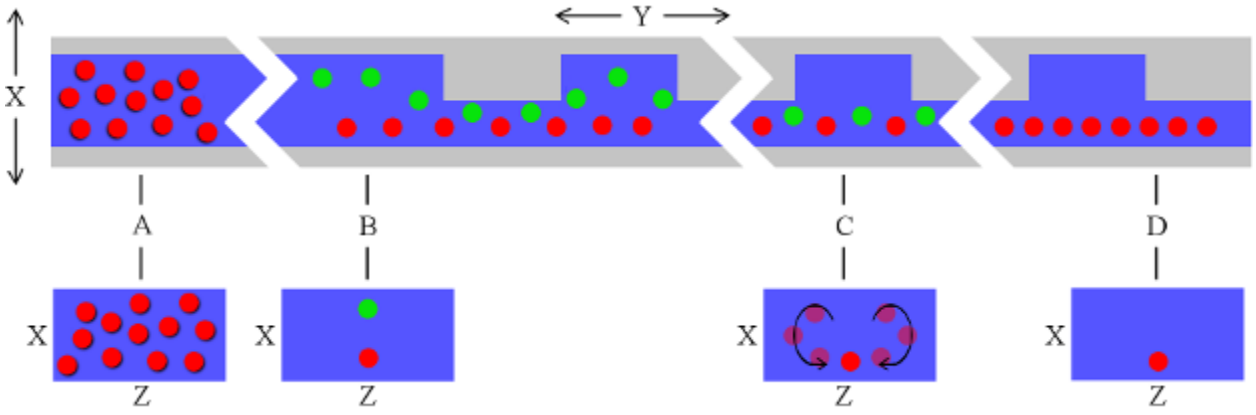

Figure 2. Schematic showing the concept behind geometry induced cell focusing. (a) Cells are injected into a microfluidic channel in random orientation. (b) Once significant distance has passed cells are ordered by lateral forces. (c) Cells then migrate due to fluid rotation in response to the stepped channels. (d) After many steps, cells are eventually ordered into a single stream near the surface of the channel.

When it is desired to detect all cells using a passive focusing method, further measures must be taken to eliminate all but one of the equilibrium positions in the microfluidic channels. This can be achieved using secondary flows induced by including a series of steps in the top of the channel [26]. Figure 2 shows a schematic for this method of cell focusing.

Initially, cells are randomly injected into the inlet of the micro-channel (Figure 2(a)), and using the concepts described in the previous section, are driven to two equilibrium positions as

denoted by the red and green dots in Figure 2(b). The steps located on the top of the channel create rotating lateral flows that compete against the previously described inertial lift forces. Cells located at the top equilibrium position (green) are susceptible to deviate from their initial positions because the induced secondary flow rotating along the perimeter of the channel is stronger than the wall lift forces acting on the cells, directing them to move downward. Once the cells approach the lower equilibrium position (red), the secondary flow becomes directed towards the center of the channel, where it must compete against strong shear lift forces imposed on the cell (Figure 2(c)). Due to this, the cells eventually become trapped in the highly stable bottom equilibrium position (Figure 2(d)) [26].

Testing using polystyrene beads (diameter 9.9 μm) has demonstrated that focusing using geometry induced flows is highly efficient, and results in a uniform single stream [26]. Furthermore it has been proven that accuracy in focusing increases with the number of successive steps. In the study by Di Carlo et al., it was found that after 25 steps a uniform stream began to appear, and after 30 steps approximately 99.77% of all particles were isolated in the bottom equilibrium position with little deviation [26].

2.4 Vertically Confined Sheath Flow

While passive techniques are capable of creating a highly focused stream of cells located within a micron from the base of microfluidic channels, they are still unable to force flows extremely close to the channel surface because cells can only exist within the naturally occurring equilibrium positions. When greater precision in directing cells to the surface is required, hydrodynamic focusing using three dimensional sheath flow can be used. Hydrodynamic focusing

is a simple technique, and the most commonly implemented method of focusing cells in current lab-scale flow cytometers [27].

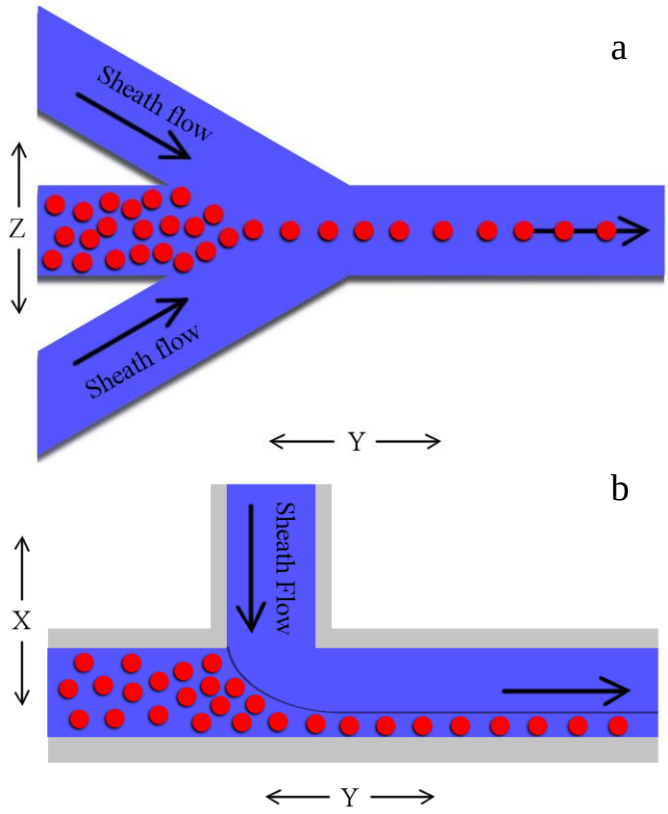

Figure 3. Concept of a microfluidic device that applies three dimensional sheath focusing to a stream of cells. (a) Cells in random order are organized into a focused stream by sheath flow in the Y-Z plane (2-D sheath flow). (b) After which, cells are forced to the surface of the channel by sheath flow in the X-direction (3-D sheath flow).

As with the previously described methods, hydrodynamic focusing requires laminar flow conditions, where streams flowing adjacent to each other show little to no lateral mixing [28]. Because of this, side streams can be added to a central stream, effectively confining the center stream between the two separate flows. In Figure 3(a), this effect can be seen for a two dimensional scenario, where cells (red) are forced to flow in a single plane due to confinement by adjacent sheath flows (2-D sheath). In a micro-flow cytometer, once cells have been 2-D focused a third

vertical sheath flow (3-D sheath) is added perpendicular to the flow of cells, effectively pushing the stream to the surface of the micro-channel, as shown in Figure 3(b).

Accuracy in focusing and controlling the height of cell streams is directly related to the ratio of sheath to sample flow rates ($R=F_{sheath}/F_{sample}$), as well as the geometry of the microfluidic device [28]. For 2-D sheath flows, the two flow rates are normally set equal in magnitude so flow of cells is directed towards the center of the channel. Additionally, effects of the 2-D and 3-D sheath flows are independent of each other, meaning 3-D sheath flow rate can be adjusted to alter vertical position of the cells without influencing the spatial confinement by the 2-D sheath flows [28].

Typically, once the microfluidic device has been fabricated, the sheath flow rates are calibrated using cells, microbeads, or tracers to determine the optimum flow ratios for the device. First, 3-D sheath flow is set to zero, and 2-D sheath flow is optimized by adjusting the flow ratio (R_{2D}) while monitoring the stream of cells under a microscope. Once an appropriate 2-D sheath flow has been set, the 3-D sheath ratio (R_{3D}) is adjusted in a similar manner until cells flow at the desired height from the micro-channel surface. In a study performed by Bashir et al. where hydrodynamic focusing was performed with channels 200 μm wide and 32 μm high, the optimum R_{2D} for focusing red blood cells was found to be $R_{2D}= 8$ [28]. When $R_{3D}= 16$ the stream was centered 3 μm from the surface of the channel (~2 μm between cell and surface), however this ratio can be increased further to force cells to flow lower.

CHAPTER 3

FINITE DIFFERENCE TIME DOMAIN METHOD

3.1 Electrodynamics Modeling

There are many important engineering concepts, such as mass transfer, energy transfer, fluid dynamics, and the propagation of electromagnetic waves that can be described by a system of partial differential equations (PDEs) with respect to both time and spatial position. For electromagnetic waves, these equations were first described by Faraday's, Ampere's and Gauss's laws for electric and magnetic fields, and later unified by James Clerk Maxwell. In their present form, Maxwell's equations are written as follows:

$$\nabla \times E = -\mu \frac{\delta H}{\delta t} - J_m \quad \text{(eq.3)}$$

$$\nabla \times H = \varepsilon \frac{\delta E}{\delta t} - J_e \quad \text{(eq.4)}$$

$$\nabla \cdot (\varepsilon E) = \rho \quad \text{(eq.5)}$$

$$\nabla \cdot (\mu H) = 0 \quad \text{(eq.6)}$$

where

$$\mathrm{E} = \left[E_x(t,x,y,z), E_y(t,x,y,z), E_z(t,x,y,z)\right] \quad \text{(eq.7)}$$

is a vector describing the strength of the electric field, and

$$\mathrm{H} = \left[H_x(t,x,y,z), H_y(t,x,y,z), H_z(t,x,y,z)\right] \quad \text{(eq.8)}$$

is the vector that describes the magnetic field strength at a specific location (x,y,z) and time (t) [29]. Furthermore, μ and ε are known as the magnetic permeability and dielectric permittivity respectively, and are properties of the material through which the electromagnetic waves are propagating [29]. The quantities J_m and J_e are the magnetic and electric conductive currents, and ρ is the charge density. In addition, the dielectric permittivity (ε) is directly related to the refractive index (n) of a material by the expression

$$\varepsilon = \varepsilon_o n^2 \quad \text{(eq.9)}$$

where ε_o is the relative permittivity [30]. Equations 3 and 4 are commonly known as the curl (∇x) equations, while equations 5 and 6 are called the divergence (∇·) equations, based on the vector operations taking place in the expressions [29]. In order to simplify these expressions, it is typically assumed that there are no conductive currents or charges within the system (i.e. $J_e = J_m = \rho = 0$). Therefore the equations become:

$$\nabla \times E = -\mu \frac{\partial H}{\partial t} \quad \text{(eq.10)}$$

$$\nabla \times H = \varepsilon \frac{\partial E}{\partial t} \quad \text{(eq.11)}$$

$$\nabla \cdot (\varepsilon E) = 0 \quad \text{(eq.12)}$$

$$\nabla \cdot (\mu H) = 0 \quad \text{(eq.13)}$$

Instead of solving this set of PDEs manually, it is common practice to implement numerical techniques to approximate values of the magnetic and electric field vectors in the spatial and time dimensions. Of the available approaches, one that is frequently used in computational electrodynamics is Finite Difference Time Domain (FDTD) analysis. In FDTD, PDEs are discretized in both time and space using central difference approximations for derivative expressions. After which, these can be solved iteratively by propagating forward in both time and

space with user defined step sizes. This iterative process is typically repeated until either a steady-state behavior is achieved, or until the user stops calculation.

Today, an increasing number of computational electrodynamics software exists, using FDTD numerical techniques. For the purpose of this study, OptiFDTD, a product of Optiwave, has been used. OptiFDTD makes a few more assumptions that allow Maxwell's expressions to be simplified even further, and will be explained in the following sections.

3.2 Two Dimensional FDTD Equations

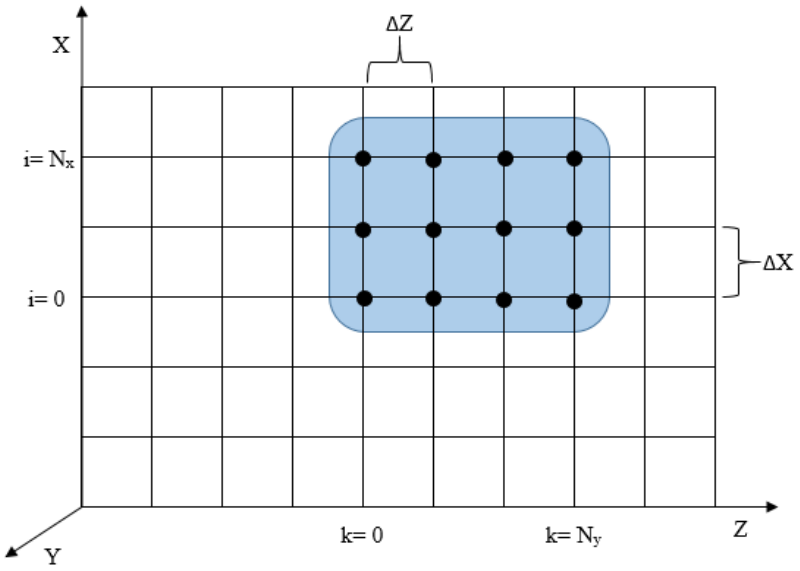

Figure 4. Representation of the computational domain in two dimensions.

While FDTD is fully capable of solving problems in three dimensions, our system only required two dimensionl simulations which significantly helped decrease calculation time. In our PhC micro-flow cytometer, simulations were performed for cells crossing a two dimensional observation plane (X-Z direction) that intersected with the PhC setup. Details of the simulations will be discussed further in chapter four. However, due to decreased dimensionality, all partial derivatives in the Y dimension can be removed, and the PDEs described by Maxwell can be

separated into two independent sets of equations depending on the polarization (TE or TM) of the electromagnetic waves. As a result, both computational time and system memory requirements were reduced for each simulation performed.

In Figure 4, the computational domain used in 2-D FDTD simulations is shown. A mesh grid created by lines spaced apart by the x-step (ΔX) and z-step (ΔZ) has been mapped across the X-Z plane, and the mesh nodes have been placed at their points of intersection (denoted by the black dots). The electric and magnetic fields are calculated within these nodes. In addition, each mesh node contains the material properties used in the approximation of Maxwell's equations, such as the refractive index of the material in which the point exists [30].

3.2.1 TE Waves

When light is polarized in a Transverse Electric (TE) configuration, electric field oscillation is permitted only in the y-dimension (E_y). This means the other values of the electric field (E_x and E_z) are equal to zero. In addition, magnetic field must always form right angles with the electric field, and as a result magnetic field oscillation can only be permitted in the x and z-directions (H_x and H_z), therefore H_y must be set to zero. By applying these polarization conditions to Maxwell's equations, the expressions previously given take on the forms [30]:

$$\frac{\partial E_y}{\partial t} = \frac{1}{\varepsilon}\left(\frac{\partial H_x}{\partial z} - \frac{\partial H_z}{\partial x}\right) \quad \text{(eq.14)}$$

$$\frac{\partial H_x}{\partial t} = \frac{1}{\mu}\frac{\partial E_y}{\partial z} \quad \text{(eq.15)}$$

$$\frac{\partial H_z}{\partial t} = -\frac{1}{\mu}\frac{\partial E_y}{\partial x} \quad \text{(eq.16)}$$

For the FDTD numerical method, each of the fields must be represented within in a two dimensional mesh that conforms to the computational domain presented in Figure 4. The nodes of

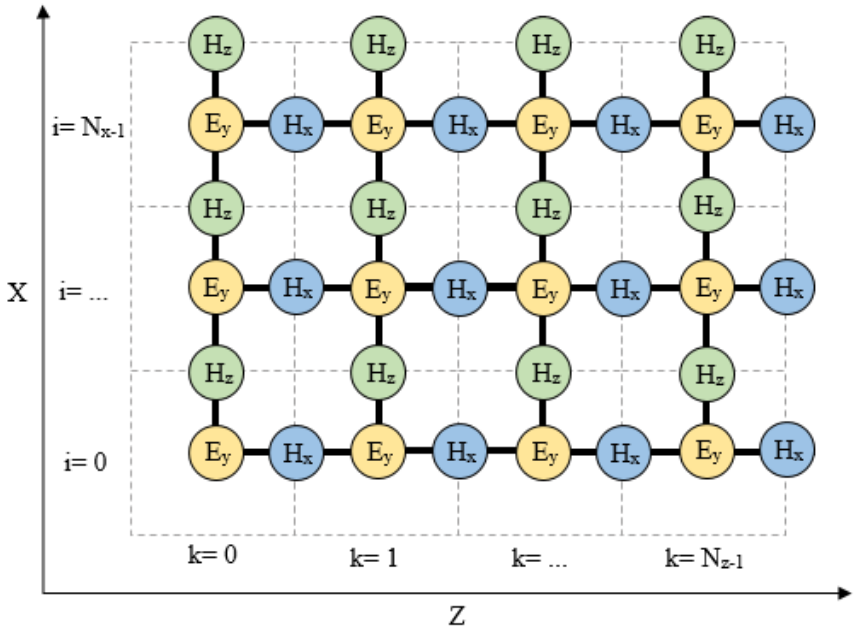

Figure 5. Location of the electric and magnetic fields within the computational domain for TE polarization.

the mesh grid are given "i and k" index notations corresponding to the space steps made in the two dimensions. For TE polarization, the position of the electric and magnetic fields is given in Figure 5. In this figure, it should be noticed that the dark solid lines correspond to the mesh grid from Figure 4, and at their intersections (the nodes) is where E_y exists. For E_y, all "i and k" indices are given integer values (i,k). The dashed lines shown in Figure 5 form what is commonly known as the "FDTD Cell," and correspond to index positions located halfway between integer values (i+1/2,k+1/2). It is along the boundaries of the FDTD cell where the magnetic fields (H_x and H_z) are calculated. The magnetic field in the x direction (H_x) is given index notation of (i,k+1/2) while the magnetic field in the z direction (H_z) has the index notation of (i+1/2,k) [30]. The strength of a field may only be calculated once the fields it is 'connected to' have been determined.

Following this index notation as well as central difference approximations for derivatives, equations 14-16 can be discretized and solved for future field strengths as follows [30]:

$$E_y^n(i,k) = E_y^{n-1}(i,k) + \frac{\Delta t}{\varepsilon}\left[\frac{H_x^{n-1/2}(i,k+1/2) - H_x^{n-1/2}(i,k-1/2)}{\Delta Z}\right]$$

$$-\frac{\Delta t}{\varepsilon}\left[\frac{H_z^{n-1/2}(i+1/2,k) - H_z^{n-1/2}(i+1/2,k)}{\Delta X}\right] \quad \text{(eq.17)}$$

$$H_x^{n+1/2}(i,k+1/2) = H_x^{n-1/2}(i,k+1/2) + \frac{\Delta t}{\mu}\left[\frac{E_y^n(i,k+1) - E_y^n(i,k)}{\Delta Z}\right] \quad \text{(eq.18)}$$

$$H_z^{n+1/2}(i+1/2,k) = H_z^{n-1/2}(i+1/2,k) - \frac{\Delta t}{\mu}\left[\frac{E_y^n(i+1,k) - E_y^n(i,k)}{\Delta X}\right] \quad \text{(eq.19)}$$

where Δt is the size of the time step, and index "n" denotes the number of time steps completed. As can be noticed from these equations, the magnetic fields not only exist halfway between spatial indices, but halfway between time steps as well. This approach to indexing is known as Yee's numerical scheme, and is frequently implemented in FDTD electrodynamic modeling [31].

3.2.2 TM Waves

Similar to TE polarization, light may also be polarized in a Transverse Magnetic (TM) configuration, where instead of electric field oscillation in the y-direction only the magnetic field is permitted to oscillate (H_y). Likewise, all magnetic field oscillations in the other dimensions are set to zero (H_x and H_z). Furthermore, electric field must only oscillate in the x and z-dimensions (E_x and E_z) where oscillation in the y-dimension is prohibited (E_y=0). Under TM polarization, Maxwell's equations may be rewritten as [30]:

$$\frac{\partial H_y}{\partial t} = \frac{1}{\mu}\left(\frac{\partial E_x}{\partial z} - \frac{\partial E_z}{\partial x}\right) \quad \text{(eq.20)}$$

$$\frac{\partial E_x}{\partial t} = -\frac{1}{\varepsilon}\frac{\partial H_y}{\partial z} \quad \text{(eq.21)}$$

$$\frac{\partial E_z}{\partial t} = \frac{1}{\varepsilon}\frac{\partial H_y}{\partial x} \quad \text{(eq.22)}$$

The representation of the FDTD cell and the locations of the fields within each is similar to the pattern shown in Figure 5, however electric fields (E_i) are replaced with magnetic fields (H_i) and vice-versa. Equations 20 through 22 may also be discretized and made solvable for FDTD methods. These equations are provided later in Appendix B.

3.3 Simulation Procedure

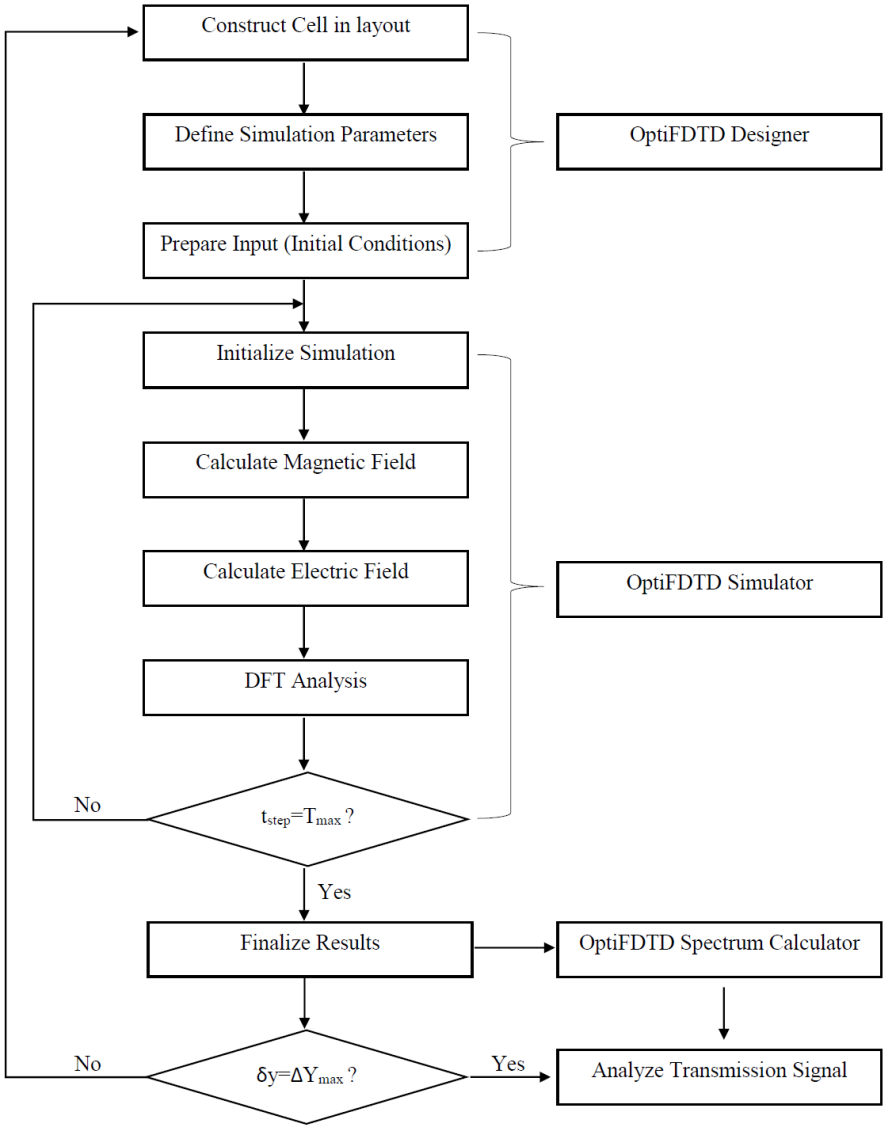

Figure 6. Algorithm for the FDTD simulation of PhC flow cytometry used in OptiFDTD.

In Figure 6, a flow diagram displaying the simulation process used in OptiFDTD is shown with respect to the PhC flow cytometry study. Within the designer software, an algorithm can be written to calculate the cross sectional geometry of a cell based on its displacement (δy) through the 2-D FDTD simulation plane. This scripting is done using Visual Basic. Once the algorithm is initiated, the designer software constructs the system layout and attributes material properties to regions within the computational domain. Next the algorithm applies the spatial mesh as well as the time constraints (ΔX, ΔZ, and T_{max}) as defined by the user, and the initial conditions (input mode) are prepared. Once this has been finished, the OptiFDTD simulator software is launched, and follows the FDTD numerical approximations described in previous sections. When the time constraint (T_{max}) has been reached the results are finalized and exported to a third program which calculates the transmission spectrum across a range of wavelengths. The algorithm is repeated continuously until the entire cell, or cells, have completely displaced through the simulation plane ($\delta y = \Delta Y_{max}$). After all simulations have been completed, the spectra calculated in each iteration are compiled into a matrix, and transmission signals are analyzed.

CHAPTER 4

DEVICE PRINCIPLES AND MODELING PARAMETERS

4.1 Note to Reader

This chapter has been adapted from work that has been previously published in *Optics Express*, 2014, 22, 12853-12860, and has been reproduced with permission from the Optical Society of America.

4.2 Device Principles

The theoretical layout of the device is presented in Figure 7(a). As with all micro-flow cytometers, initially the cell sample is spatially focused into a narrow stream of individual cells. As demonstrated in the chapter 2, spatial focusing of cells can be achieved through several well studied techniques such as hydrodynamic focusing with a sheath fluid, or through sheath-free inertial focusing methods [26,28,32]. Regardless of the procedure applied, the cells must be focused for the device to behave as desired. As has been shown, studies on the vertical positioning of cells have demonstrated a capability to push cells extremely close to the surface of a microfluidic chamber using a sheath fluid [28]. In addition, the current PhC configuration is slightly raised from the surface of the micro-channel (0.6 μm). With this in consideration, cells were modeled close to the PhC surface to allow for greater interaction with the structure. Once the cells have been properly aligned, the stream flows over the surface of a 1-D PhC where individual cells will

interfere with the transmission of light through the crystal. By studying the change in the transmission spectrum, information regarding the cells can be determined.

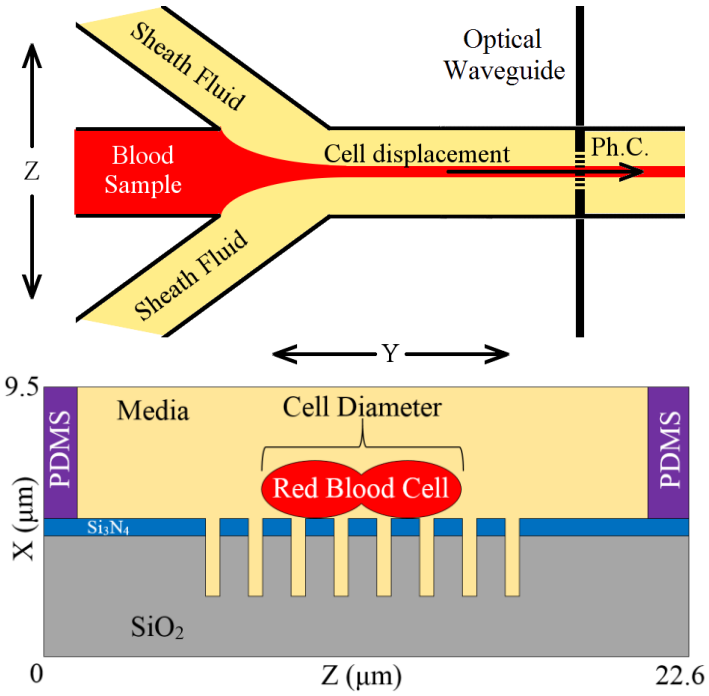

Figure 7. Theoretical layout of the device on chip. (a) Cell focusing using a sheath fluid is conducted on the left and optical detection using a PhC is on the right. (b) Cross sectional layout of the PhC as seen from FDTD simulations with blood cell present

4.3 Modeling Parameters

The device was designed and simulated in 2-D with OptiFDTD [33] to model the propagation of light through the photonic crystal. A general schematic of the PhC cross section is represented above in Figure 7(b). The PhC consists of two materials, a 0.6 μm thick layer of silicon nitride (refractive index 2.03) shown in blue [34], and silicon dioxide (refractive index 1.54) shown gray [35], serving as a cladding. The design of the PhC includes periodic slits patterned in the nitride layer 0.5 μm wide and 2.7 μm deep. Spacing of each slit was 1.5 μm from their center, with a total of eight slits over the entire PhC. Cells are guided towards the photonic crystal through microfluidic channels, 20 μm wide, created by a layer of PDMS (refractive index 1.41) shown in

purple (Figure 7 (b)) on both the left and right sides above the silicon nitride structure [36]. The structure was then considered completely filled with a liquid medium for analysis, shown in yellow (plasma with the refractive index 1.3515 [37]). The medium was allowed to fill the slits. Because interactions between the surface of the PhC and the cells occur within a plane located parallel to the y-dimension, it is preferred to calculate electric fields that oscillate within the same direction. Because of this, light was polarized using a TE configuration, allowing for calculation of E_y.

Initially, the sensitivity of the PhC in different spectral regions was tested to determine the wavelengths of light which would be most appropriate for optimum detection of cells. In order to study the PhC sensitivity, a silicon nitride cantilever tip was simulated to probe different regions of the crystal while transmission spectra were calculated. The probe tip was permitted to touch the crystal surface, while the resulting change in the transmission spectrum was recorded for the current tip position, and repeated over entire length of the PhC.

Once the appropriate wavelengths for scanning were determined, the flow of red blood cells was simulated and change in transmission was monitored at these wavelengths. Red blood cells were used as they are among the smallest cells found in the human body with complex and interesting geometries. Blood cells varied in size from 6 to 8 μm in diameter [38]. Initial tests were performed for cells of a consistent refractive index (1.387), and then later further complexity was added to the model, where refractive index of cells varied from 1.387 to 1.401 in accordance with the acceptable range from literature [39,40].

Flow of cells was modeled based on the incremental displacement (δy) of the cells through an observation plane in the 2-D FDTD model (x and z directions), where the geometry of cell cross-sections based on incremental displacement of the cell were calculated and simulated for each iteration as the cell moved through the plane of study. The geometries of these 2-D cell cross

sections were calculated under the assumption that blood cells may be approximated as biconcave discs, whose cross section is composed of overlapping ellipses as seen in Figure 7. In addition, each blood cell was assumed to be perfectly symmetric around the center. Therefore, displacement for a single cell only had to be calculated from the center (δy=0 μm) to the edge of the cell (δy =R μm). Due to the symmetry assumption, results were reflected across the origin to visualize the effects of the entire cell movement through the observation plane. In practice, if the cells are not symmetric due to, for example, sickle cell disease, this asymmetry will be detected in the measurements of transmission signals. Furthermore, the refractive index of the surrounding media was assumed to be held constant for the duration of each simulation.

CHAPTER 5

1-D PHOTONIC CRYSTAL BEHAVIOR

5.1 Note to Reader

Portions of this chapter have been adapted from work that has been previously published in *Optics Express*, 2014, 22, 12853-12860, and has been reproduced with permission from the Optical Society of America.

5.2 Analysis of Transmission Spectra

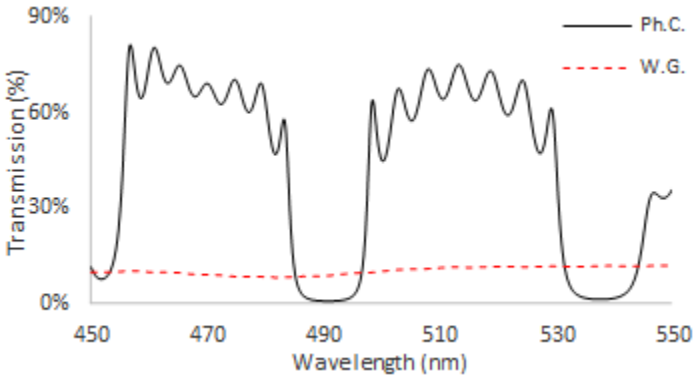

Figure 8. Calculated transmission spectrum of the PhC (black) as compared to a disrupted optical waveguide (red) of equal thickness.

In order to apply this micro-flow cytometer to plasma and whole blood analysis, the initial spectrum was calculated for the PhC device fully immersed in plasma (refractive index 1.3515) (Figure 8). From this spectrum, the band gaps and regions of high transmission can be clearly identified. Electric field distributions (Ey) are provided in Figure 9 for two different wavelengths.

At a wavelength of 490.0 nm, light is incapable of transmitting through the crystal, which corresponds to the bang gap region as seen in Figure 8, while at a wavelength of 513.3 nm light is going through.

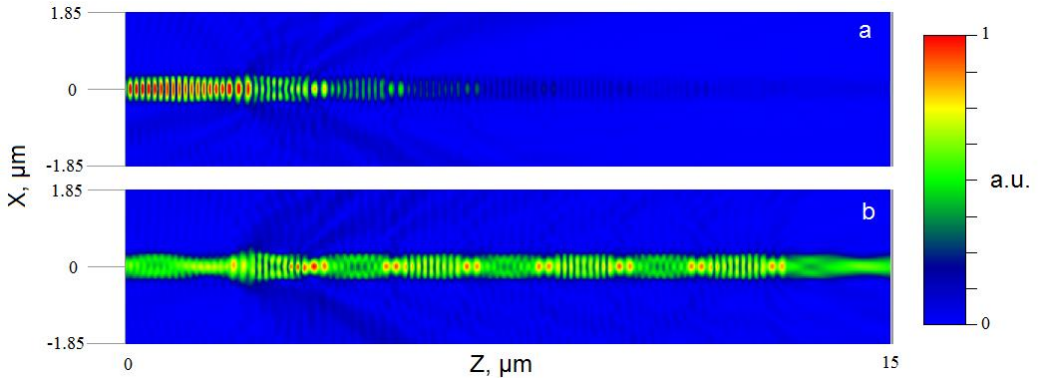

Figure 9. Electric field (E_y) distribution through the PhC immersed in plasma for the (a) Band gap wavelength 490.0 nm, and (b) Peak transmission wavelength 513.3 nm.

Different regions of PhC spectra can be used for different applications – the same device may operate at multiple wavelengths, all of which provide comparable information and may be interchangeable if additional channels of detection (e.g. fluorescence) are needed. For example in Figure 8, the wavelength region 455-485 nm may be used for counting and assessing cells as they flow past the device, while the second region shown (495-532 nm) may be used to perform fluorescent studies with dyes that emit light at those specific wavelengths. Once the size of the cell has been determined from the first region, a baseline transmission can be extrapolated for the entire spectrum based on the models of non-florescent cells. Any increase in transmission due to emission from fluorescent dyes in the second region may then be quantified for the expression study.

Additionally, in Figure 8, transmission through the PhC is compared to that of a "disrupted" optical waveguide, a component previously proposed for micro-flow cytometry devices [11]. This disrupted waveguide was simulated for the same materials and dimensions as layers of the PhC and it may be clearly seen that transmission in the PhC is exceedingly greater than what is observed

with the disrupted optical waveguide. In order to increase transmission, the disrupted waveguide has to be significantly larger, but this would considerably decrease the resolution of the device, since it is inversely proportional to the dimensions of the optical components. Ideally, a component with dimensions smaller than that of a cell would be needed for a proper detection. Therefore smaller devices capable of achieving high transmission, such as the PhC are preferred to larger optical waveguides.

5.3 Effects of Surrounding Media

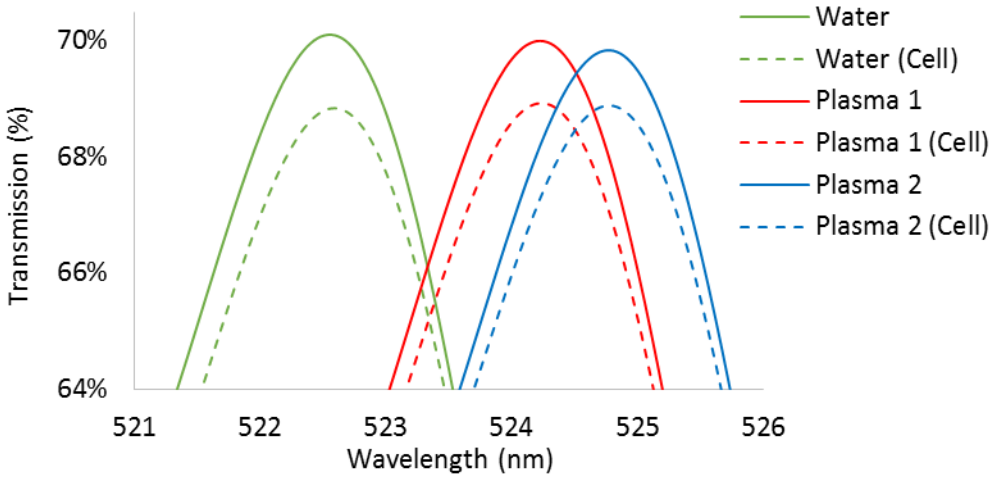

Figure 10. Peak transmission spectrum for different media, with and without a red blood cell.

To characterize influence of media refractive index on the photonic crystal spectrum, the first set of simulations was conducted in absence of the cells and compared to those when a cell (d=7μm) was present in different media. Three media were compared: water (refractive index 1.333), and two blood plasma samples with slightly different refractive indices (1.3515 and 1.3575) [37]. Figure 10, shows the effects on transmission spectrum when a blood cell is present on the PhC surface, as well as a response to a change in the surrounding media. While changes in transmission are observed over the entire spectrum, here attention is focused on a narrow region

where maximum transmission is occurring. These regions of maximum transmission are where the influence of cells and media are the strongest and the most evident. The central wavelength of maximum transmission is directly related to the refractive index of the surrounding media. Water with the lowest refractive index corresponds to peak transmission at a shorter wavelength, while Plasma 2, the highest refractive index fluid, has a peak transmission at longer wavelength. Furthermore, the central wavelength of maximum transmission is not influenced by presence of the cell on the surface. It only effects transmitted light intensity. Based on this, it is possible to not only detect cell presence or absence, but also independently measure the refractive index of the surrounding media. Plasma (refractive index 1.3515) was used as the surrounding fluid for the remainder of the study.

5.4 Photonic Crystal Surface Sensitivity

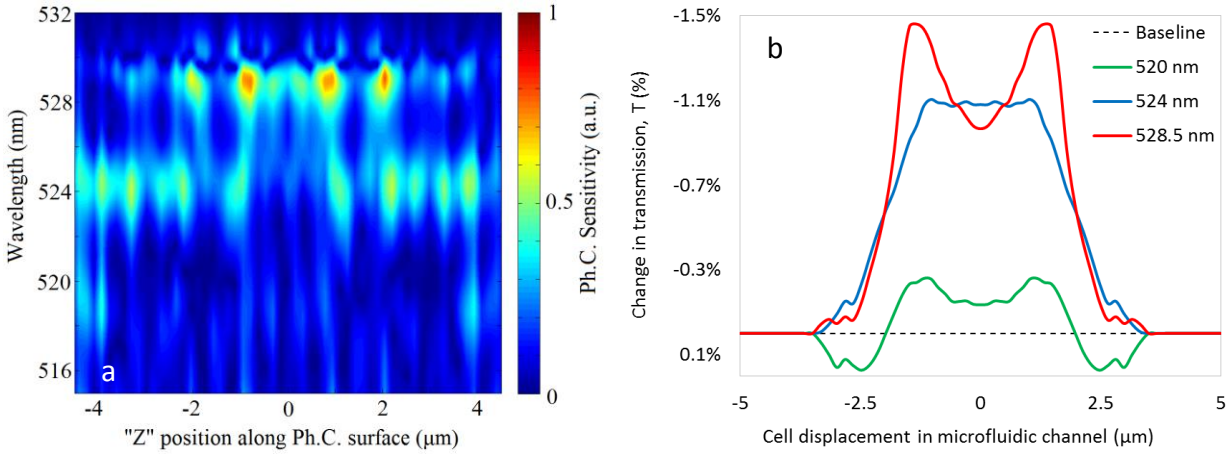

Figure 11. Sensitivity of the PhC at the surface. (a) Heat map showing regions where the PhC is sensitive to light scattering, over the spectrum range 515-532 nm. (b) Change in transmission due to a blood cell (diameter: 7 µm, refractive index: 1.387) is shown for three wavelengths exhibiting notable sensitive regions on the PhC surface (521, 524, 528.5 nm).

Results of the PhC sensitivity study are shown in Figure 11(a). The heat map displays amplitude of the scattering losses for a range of wavelengths (515-532 nm), as well as the

corresponding location on the PhC surface. Here, sensitivity values of 1 correspond to the wavelengths with the maximum light scattered from the crystal, while 0 indicates that transmission was unaffected. From Figure 11(a) it may be clearly noticed that distinct regions with higher sensitivity to the presence of an object form along on the crystal surface for specific wavelengths of light.

There are three wavelengths corresponding to high sensitivity patterns - 520, 524 and 528.5 nm. For light at 520 nm, the PhC is in its least sensitive regime, which is clearly reflected in low changes of transmission while detecting a red blood cell (diameter: 7 μm, refractive index 1.387) presented in green for Figure 11(b). Such wavelengths with low sensitivity might not be appropriate for analyzing cell properties, however they might still be useful for performing fluorescent studies with dyes that emit light at those wavelengths. However, at a wavelength of 524 nm, the crystal becomes moderately sensitive to objects near the surface, yet these sensitive regions are located along the left and right sides of the PhC and not at the center where flowing cells would be spatially focused by the microfluidic system. As a result, cells are being scanned not in the center, but along the lobes and edges and thus shape is not reproduced. (blue curve in Figure 11(b)). The most sensitive wavelength of light, in this study, was found to be approximately 528.5 nm. In Figure 11(a) at this wavelength, the region of the PhC most susceptible to influence by objects at the surface is roughly located around the center of the crystal. As a result, the signal corresponding to the flow of the red blood cell has the highest amplitude in Fig, 5(b) and also spatial information is preserved and the concave disc shape can be observed. As this wavelength provided the most well defined and strongest signal for the cell detection, 528.5 nm was used for the remainder of this study.

CHAPTER 6

MICRO-FLOW CYTOMETRY RESULTS

6.1 Note to Reader

Portions of this chapter have been adapted from work that has been previously published in *Optics Express,* 2014, 22, 12853-12860, and has been reproduced with permission from the Optical Society of America.

6.2 Desired Functions

Once cells were permitted to flow across the surface of the PhC, changes in transmission were recorded over the relevant spectrum. Figure 12 shows a heat map displaying changes in transmission for a single 7 μm blood cell with respect to both the wavelength of light propagating through the device, as well as the displacement of the cell through the plane. For some wavelengths, e.g. around 524 nm, the blood cell appears to scatter light resulting in overall decrease in transmission, while for other wavelengths, e.g. near 531 nm, the blood cell appears to act as a cladding layer, which actually causes an increase in the transmission through the PhC.

After validating the ability to detect presence of the cell, the next step is to demonstrate that a PhC micro-flow cytometer is capable of replicating the some of the primary functions of lab-scale flow cytometry units. These desired functions are namely: the ability to count cells, to characterize cell shape, as well as determine the size of the cell.

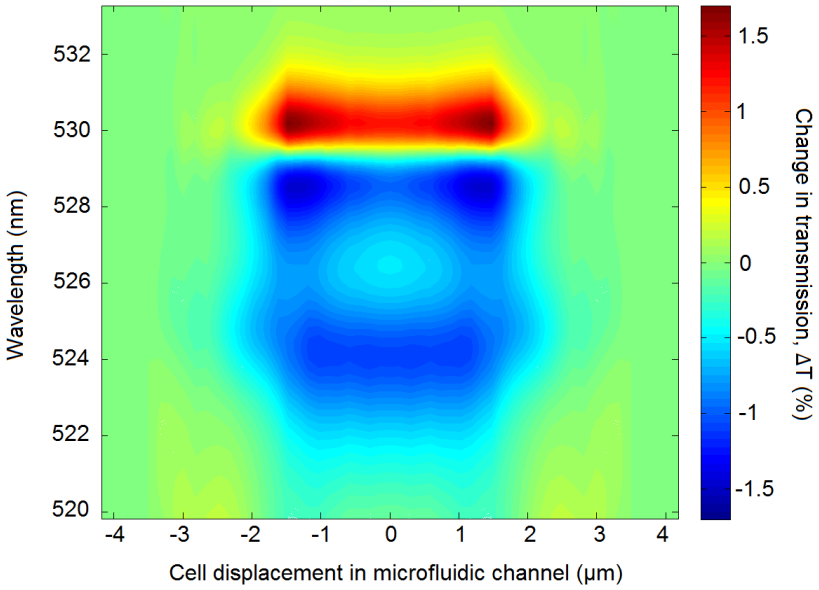

Figure 12. Heat map displaying difference in transmission caused by cell movement (d=7μm) for the spectral range 520-533 nm.

6.3 Cell Counting

In order to demonstrate counting, three blood cells of different diameter (6, 7, and 8 μm respectively) were flowed through the device. The simulation was designed such that no space existed between any two cells flowing consecutively in a line through the device, and each sequential blood cell was in direct contact with its neighboring cells as they passed over the PhC surface. Since cells have a natural tendency to sediment, and hydrodynamic focusing can be used in experiments, an assumption was made that cells can always be flowing close to the surface. Changes in transmission (ΔT) were recorded and plotted against the cumulative displacement of the cell stream as it passed through the device. In practice, measurements would be recorded with respect to time, and converted into displacement by multiplying time with the velocity of the cell stream. Displacement is used for the plots as it may be easily correlated to the dimensions of the cells. The simulation results are shown in Figure 13 for a wavelength of 528.5 nm. It can be seen

that a characteristic change in transmission was detected as each cell passed through the observation plane. The fact that distinct signals existed for each of the cells demonstrates the capability of such a device to count cells flowing in series. While, the degree to which each cells can be resolved from one another is dependent on the width of PhC, and as previously shown, this device is able to function at dimensions that are only fractions of a cell diameter.

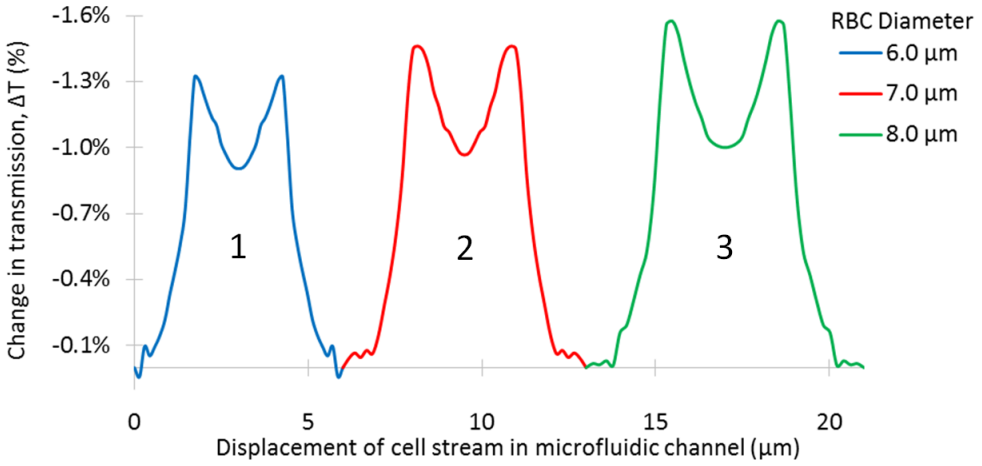

Figure 13. Transmission change corresponding to three cells flowing in series, detection conducted at λ= 528.5 nm.

6.4 Shape Characterization

In Figure 14, change in transmission due to cell movement is shown for two different shapes. One of them was a 7 µm blood cell, and the other a white blood cell (Refractive index 1.42, diameter 12 µm [41]). Significantly different signal distributions were observed for the two cell types. For the red blood cell, the change in transmission exhibited a symmetric double peaked distribution, while for the white blood cell, the signal was more normally distributed around the center. Comparing signal distribution for the red blood cell to the cross sectional image of the as seen in Figure 7(b), a connection between the shape of the signal and the physical object can be observed. Thickest portions of the object, such as the center of the cell 'lobes' display the greatest

effect on transmission in the PhC, while locations of the cell with lower thickness such as the center and edges of the cell have less of an effect overall. Based on this, it can be clearly seen that information regarding cell shape may be extracted with photonic crystal micro-flow cytometry.

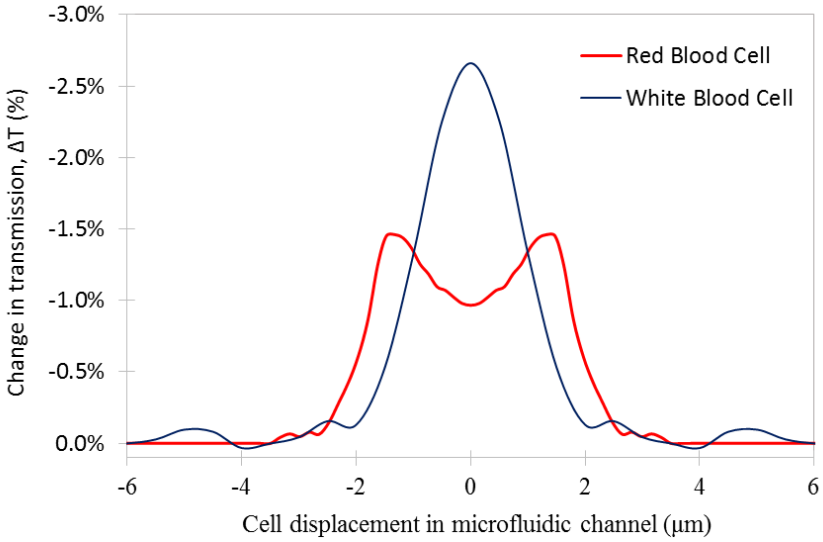

Figure 14. Change in transmission for different cell types – red blood cell (red) and white blood cell (blue), λ= 528.5 nm.

6.5 Cell Size Correlations

6.5.1 Constant Refractive Index

Finally, a correlation between red blood cell size and change in transmission was required to achieve a working model for a functional micro-flow cytometer. In order to accomplish this, blood cells ranging from 6 to 8 μm in diameter were analyzed with the proposed device. Figure 15(a) represents the change in transmission ΔT measured at a wavelength of 524.1 nm for each of the cells in relation to their displacement through the observation plane δy. It can be noticed that as blood cell diameter increased, the overall area under the corresponding transmission signal increased as well. The area under each transmission curve was determined through numerical integration and plotted as a function of displacement δy in Figure 15(b). Results for the areas under

each curve were then plotted against their corresponding blood cell diameter (Figure 15(c)). Based on the coefficient of determination R^2, there is a strong correlation between the transmission area and the red blood cell diameter.

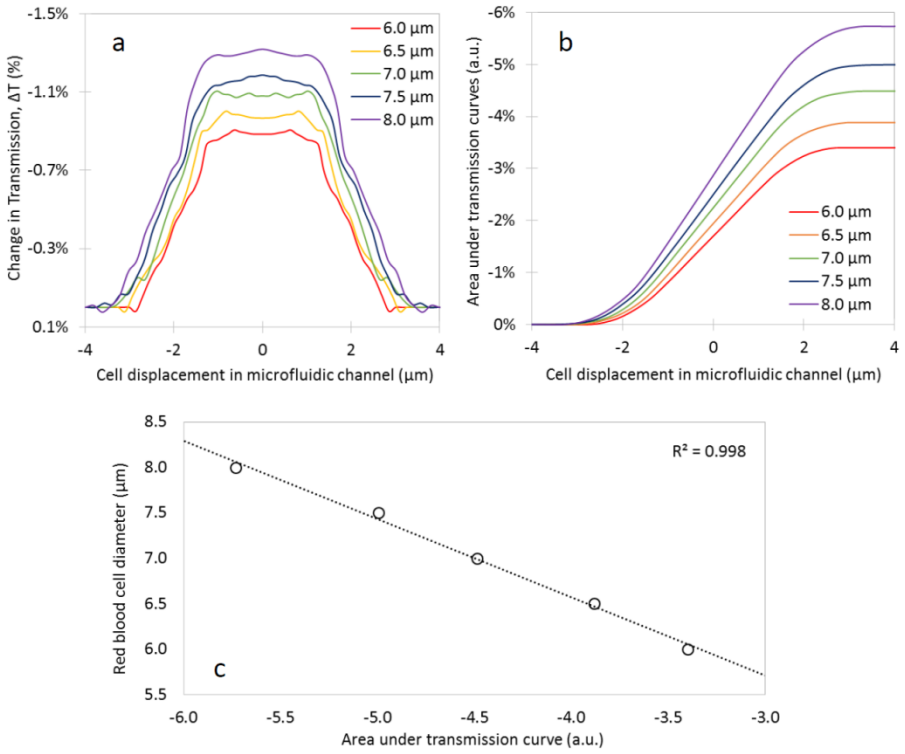

Figure 15. Change in transmission for cells of different size, λ= 524.1 nm. a) Change of transmission for blood cells of various diameters (6-8 µm) w.r.t. cell displacement in the microfluidic channel. b) Numerical integration of area under transmission change curves. c) Correlation between blood cell diameter and the area under the transmission change curves.

6.5.2 Variable Refractive Index

As previously shown, research of PhC transmission signals have demonstrated a capability to determine characteristics of cells as they flow past the surface of the crystal [42]. However, these findings were performed for cells of a fixed single value of refractive index. Furthermore, as with most biological substances, refractive index can vary over a certain range, and is not consistent from object to object. For blood cells, this range is approximately 1.387 to 1.401 [40].

Despite the added variability in refractive index, characterizing cells with photonic crystals can still be performed using additional analysis and statistical methods.

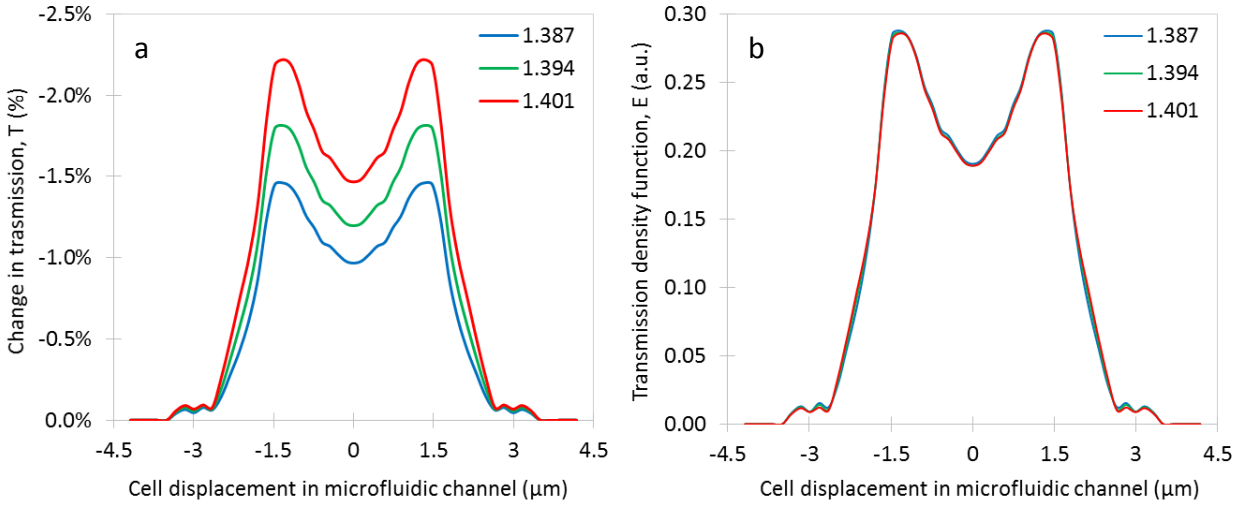

Figure 16. Characteristic signals of red blood cells (diameter: 7 μm) with varying refractive indicies. (a) Change in transmission at a specific wavelenghth from PhC spectra is shown for the three cells. (b) Transmission signal after transformation into transmission density functions. λ=528.5 nm.

In order to observe the influence of cell refractive index on the resulting transmission signals (*T*), blood cells with average refractive indices of 1.387, 1.394 and 1.401 were modeled for the range of diameters of cells (6-8 μm). Change in transmission (*T*) of the PhC for 7 μm blood cells over the range of possible refractive indices are shown in Figure 16(a). It may be noted that for variations in refractive index the only significant difference between each transmission signal is with the amplitude of the signal. As the cell refractive index increases, more light is scattered from the PhC, yet the overall shape of the signal appears to be completely unaffected. Each of the recorded transmission signals (*T*) were then transformed into transmission density functions (*E*) by using the following expression [43]:

$$E(y) = \frac{T(y)}{\int_{-\infty}^{\infty} T(y)dy} \qquad \text{(eq.23)}$$

where *E* and *T* are both functions of cell displacement in the microfluidic channel (*y*). Results of this transformation have been plotted for the same 7 μm diameter blood cells, presented in Figure 16(b). It can be clearly seen that upon converting the data into transmission density functions, the effects of blood cell refractive index appear to vanish, as each density function (*E*) displays approximately the same distribution with only minor differences. Because of this, statistical analysis of transmission density functions using the theorem of central moments could be applied, providing a reliable technique for measuring cell characteristics when variations in refractive index arise in photonic crystal micro-flow cytometry.

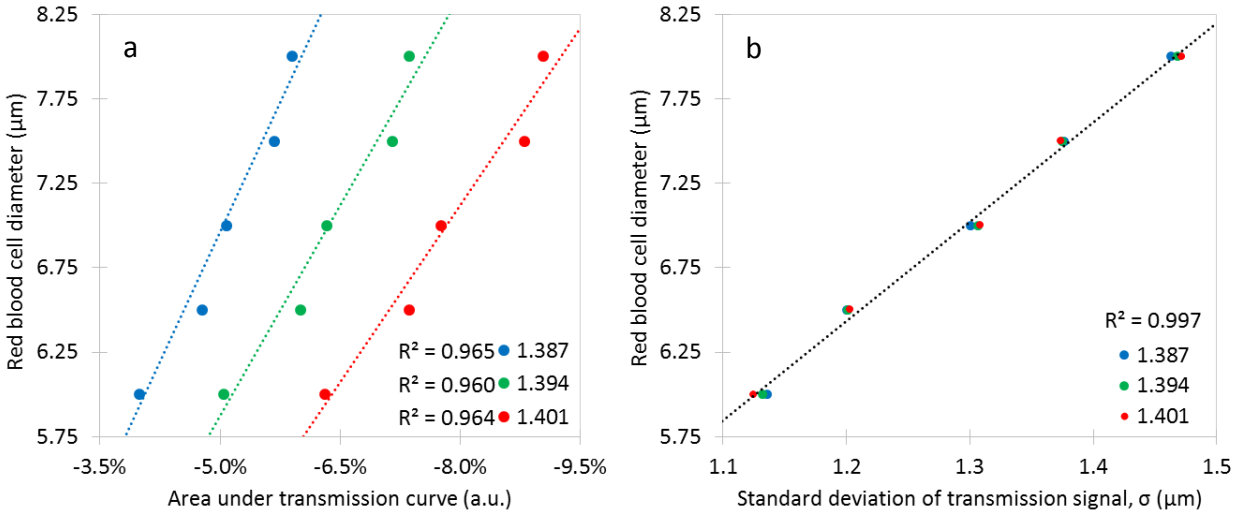

Figure 17. Method for determining blood cell diameter. (a) Relationships between cell diameter and area under transmission curves are no longer effective once refractive index can change. (b) By applying theorem of central moments, a strong correlation exists between blood cell diameter and the resulting standard deviation of their transmission signals (μm). λ=528.5 nm.

Prior studies of some cell parameters with photonic crystal flow cytometry showed that there is a strong correlation between the areas under transmission signals and the diameters of the objects passing over the crystal surface [42]. Using this information, it is possible to obtain the size of objects by integrating their transmission signals. Nonetheless, for blood cells and other biological entities, where refractive index is unknown and not consistent for each cell being

studied, integration of transmission signals is no longer sufficient for determining the size of the cells.

In Figure 17(a), area under transmission curves for blood cells of various refractive indices have been plotted against their corresponding blood cell diameters. Data shown in blue corresponds to blood cells with a refractive index of 1.387, points in green are cells with refractive index of 1.394 and points in red are cells with refractive index of 1.401. Relationships between the transmission signal areas and blood cell diameters do exist, as indicated by the dashed lines, however these only occur among cells with the same refractive index. In addition, these individual relationships for cells with constant refractive index only exhibit moderately strong linear correlations, as the data appears to oscillate above and below the lines of best fit.

In order to resolve the issues that arise when cell refractive index can vary, we will apply the equations for the first and second central moments, given in equations 24 and 25, on the previously described transmission density functions (*E*) [43].

$$\overline{y} = \frac{\int_{-\infty}^{\infty} y \cdot T(y)dy}{\int_{-\infty}^{\infty} T(y)dy} = \int_{-\infty}^{\infty} y \cdot E(y)dy \qquad \text{(eq.24)}$$

$$\sigma^2 = \frac{\int_{-\infty}^{\infty} (y-\overline{y})^2 \cdot T(y)dy}{\int_{-\infty}^{\infty} T(y)dy} = \int_{-\infty}^{\infty} (y-\overline{y})^2 \cdot E(y)dy \qquad \text{(eq.25)}$$

Here, $\overline{y}$ is the first central moment, otherwise known as the average displacement (μm). For symmetric distributions such those found in our blood cell model, the average displacement simply corresponds to the displacement at the center of the signal. The value of $\overline{y}$ holds no major significance at this point, but must be determined for later calculations. In Figure 16(b), it may be clearly seen that the value of $\overline{y}$ is 0 μm, however this is only due to the nature of the simulations in this study, and would not be 0 μm in practice. In application, multiple transmission signals of several cells would be continuously collected and recorded with respect to time. Time can then be

converted into displacement values through multiplication by the velocity of cells passing across the PhC surface. Each individual signal would then be numerically processed by computer software using these equations. For experimental data the average displacement must be calculated for each signal studied.

Once average displacement is known, the second central moment σ^2, known simply as the variance, could be calculated using equation 25. In Figure 17(b), the standard deviation (square root of variance) of the transmission signals are plotted with their corresponding blood cell diameters, as well as their refractive index. It can be noticed that a significantly stronger correlation (R^2 = 0.997) between the cell diameter and signal standard deviation appears when compared to the previous results in Figure 17(a), and this linear relationship agrees for the range of blood cell refractive index studied. Using this relationship, as well as the previously mentioned equations, transmission signals collected from a PhC device can be used to determine the diameter of a blood cell, regardless of the cells refractive index.

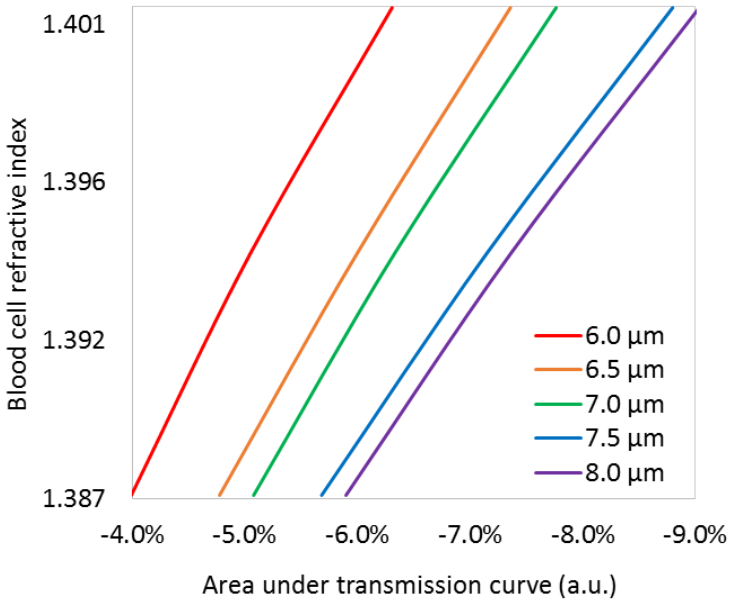

Figure 18. Blood cell refractive index as a function of the area under transmission change curves for known cell diameters. λ=528.5 nm.

After the size of the cell has been determined with the above mentioned techniques, it is then possible to calculate the refractive index of the cell by analyzing the original transmission signal (*T*), such as those shown in Figure 16(a). In Figure 18, blood cell refractive index is shown with respect to resulting areas under transmission curves, for all cell diameters studied. By using this plot, the refractive index can be obtained by integrating under transmission curves, and since diameter is already known the line that must be followed can also be determined.

CHAPTER 7

FURTHER CONSIDERATIONS AND RECOMMENDATIONS

7.1 Spatial System Resolution

One important requirement for high quality device operation is for micron, and even sub-micron resolution, in order to be able to resolve details of the signals from individual cells. In PhC micro-flow cytometry, resolution is directly related to the width of the PhC. This correlation between system resolution and the width of the PhC was studied using three dimensional FDTD simulations.

In this set of simulations three identical blood cells, all 7 μm in diameter with a refractive index of 1.387, were passed through the PhC system previously described in Chapter 4, where the only variable among each simulation was the width of the PhC. Cells were passed in a focused stream, and neighboring cells were in direct contact with each other. This cell spacing orientation was used as a worst case scenario, where resolving individual cells would be challenging for even the most robust micro-flow cytometers. However, in practice some space would exist between cells depending on the focusing technique applied.

Results of the study are provided in Figure 19, where the effects of PhC width on resolution may clearly be seen. Notice that for a PhC width of 1 μm (Figure 19(a)), an achievable dimension for fabrication, each individual signal is still distinguishable and geometric features of the cell are still visible in the transmission signal distribution. However, as PhC width increases to 2

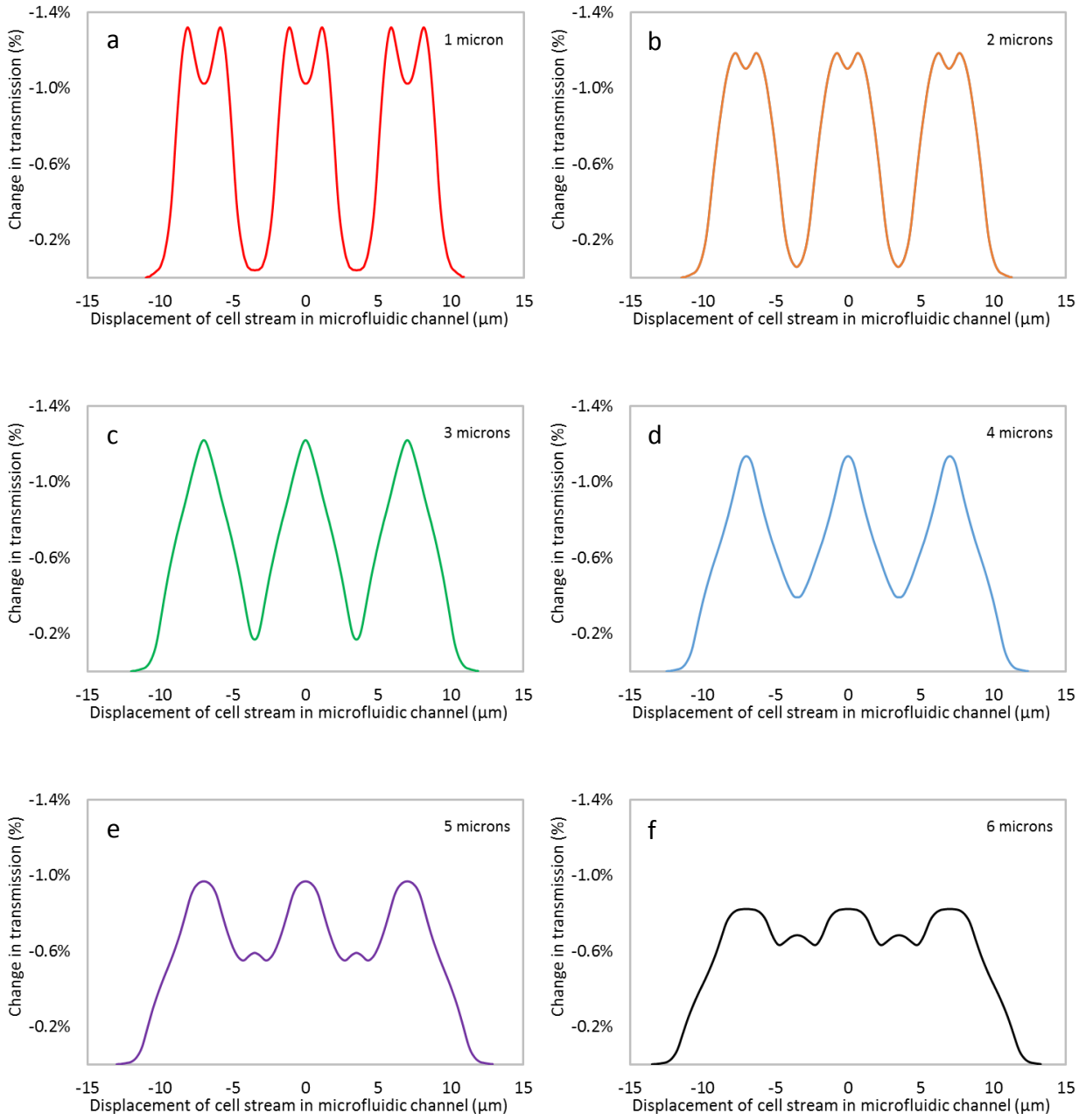

Figure 19. Transmission signals of three blood cells flowing in series for PhC flow cytometers with varying waveguide widths. (a) 1 µm. (b) 2 µm. (c) 3 µm. (d) 4 µm. (e) 5 µm. and (f) 6 µm.

µm (Figure 19(b)), the geometric cell features begin to diminish, until by 3 µm (Figure 19(c)) they are unnoticeable entirely. These larger PhC widths would be suitable for general micro-flow cytometer operations, such as counting, and potentially size correlation, however at this point

distinguishing cell shape would become impossible (for blood cells). At widths of 4 μm (Figure 19(d)), resolution is significantly reduced to the point that individual signals are beginning to blend with one another. Because of this, correlating cell size using techniques described in Chapter 6 would most likely be impossible, while counting is still applicable. Eventually, by widths of 5 μm and 6 μm (Figure 19 (e) and (f)), resolution is diminished so greatly that the signals become completely unrecognizable from one another and PhC micro-flow cytometry would be impossible to perform for cells of this size.

Since there is a trade-off between cost of fabrication for smaller features and decreased resolution for larger ones, the width of the PhC should be 1 μm. This width would provide good optical resolution, while it can still be fabricated at a relatively low cost. Furthermore, PhC width and resolution is entirely related to the application and type of cell being studied. In these models, red blood cells were used as they are among the smallest cells found in the human body with complex and interesting geometries. As a general assumption, if characteristics of a red blood cell (6-8 μm diameter) may be resolved, then it would definitely be possible to resolve signals for other eukaryotic cells, which typically range from 10-100 μm in diameter. The only caveat being that the microfluidic channels need to be designed wide enough to permit the flow of larger cells through the device.

7.2 Proposed Fabrication Techniques

After proposing a new theoretical design of a photonic crystal micro-flow cytometer, the next step is to determine potential fabrication procedures (Figure 20). Each fabrication step is described below in several subsections. The photonic crystal and the microfluidic components are fabricated separately, after which they are bonded together to form the fully assembled device.

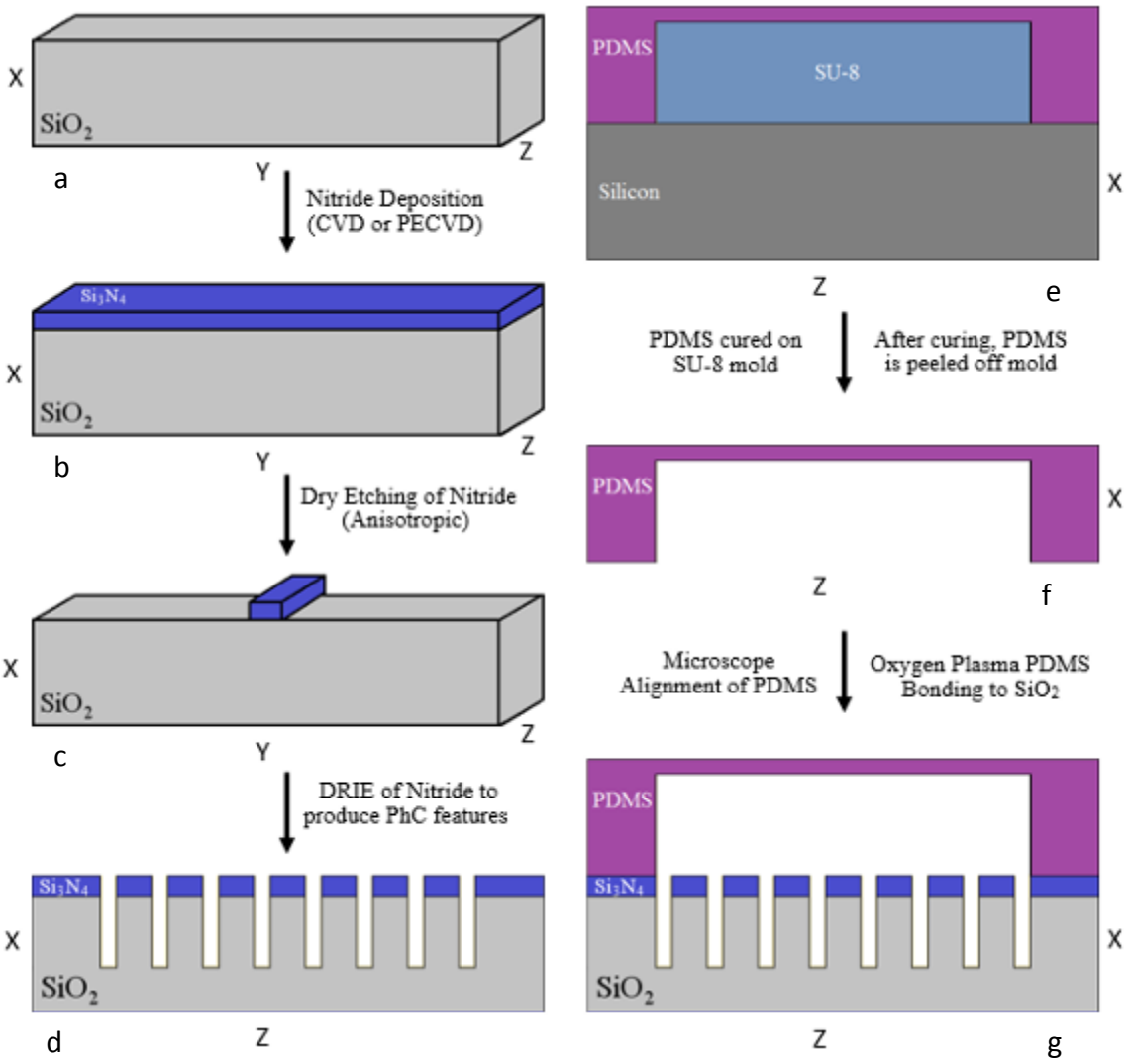

Figure 20. Process flow diagram for the fabrication and assembly of the PhC micro-flow cytometer. Not drawn to scale.

7.2.1 Silicon Nitride Deposition

In order to create the photonic crystal, a layer of 0.6 μm silicon nitride must first be deposited onto a glass substrate (Figure 20(a)). Nitride deposition can be performed by two techniques: Low Pressure Chemical Vapor Deposition (LPCVD) or Plasma Enhanced Chemical Vapor Deposition (PECVD) [44]. The primary difference between these two processes is the method by which the gas phase reactants are transported to the substrate surface. In LPCVD,

transport of the gas is dominated by diffusion due to concentration gradients within the reactor. The reactor is maintained at low pressures (10-1000 Pa), where the flux of gas to the surface is significantly reduced [45]. As a result, the deposited nitride films will be more uniform and homogeneous [46]. In PECVD, two electrodes, in parallel plate configurations, are added to the reactor, and the substrate is placed on the lower electrode. Partially ionized gas (plasma) is then combined with the reactants in the space between the electrodes. By applying a voltage, the plasma becomes excited and causes the reactive gas to dissociate and deposit on the substrate [45]. In either process, gaseous silane (SiH_4) and ammonia (NH_3) are introduced to the reactor. Once the reacting species adsorb to the substrate surface, the reaction occurs ($3\ SiH_4 + 4\ NH_3 \rightarrow Si_3N_4 + 12\ H_2$) and newly formed silicon nitride is deposited on the substrate (Figure 20(b)). Nitrides deposited via this reaction produce large quantities of hydrogen, which may bond to silicon or nitrogen and can potentially influence the optical properties of the nitride for infrared and ultraviolet wavelengths [47]. However, since the proposed device operates in the visible light spectrum, this should not have any impact on the functionality of the micro-flow cytometer.

7.2.2 Lithography and Silicon Nitride Etching

Once silicon nitride has been deposited, excess nitride needs to be removed and 1 μm waveguides can be patterned. This is achieved by photolithography and dry etching of the nitride. Here, dry etching is preferred over wet etching because of its ability to produce vertical edges due to anisotropies in the nitride layer [48]. First, the nitride is coated in a photoresist, such as SU-8 (a negative resist) which is pre-baked, exposed to UV light through a needed mask, post-baked and then developed using SU-8 developer. Upon exposure to UV light, SU-8 crosslinks and solidifies, becoming insoluble to the photoresist developer. The areas protected by the mask may then be dissolved in the developing solution, leaving behind a strip of SU-8 on the surface of the nitride.

This SU-8 feature protects the 1 μm wide region of nitride during the dry etching process. In dry etching, nitride is then bombarded with ions (typically reactive plasmas), that gradually remove the exposed material [48]. Once the process is completed, the SU-8 protective strip can be removed, leaving behind the thin silicon nitride waveguide structure (Figure 20(c)).

To create the photonic crystal features (i.e. the periodic channels etched through the nitride layer) we must follow a procedure similar to the one previously described, however, due to the sub-micron features we wish to pattern, electron beam (e-beam) lithography followed by deep reactive ion etching (DRIE) should be used. For e-beam lithography, the silicon nitride waveguide structure shown in Figure 20(c) is first covered in an e-beam resist (thin layer of PMMA), which changes solubility to a developing solution upon exposure to an electron beam [49]. The electron beam then patterns features in the resist that correspond to the photonic crystal channels (0.5 μm wide, spaced 1.5 μm between centers). After rinsing with a developer, the portions of the PhC that are not desired to be etched are protected by the electron sensitive resist. Next, DRIE is performed on the protected waveguide to create the 2.7 μm deep, vertical slits of the PhC. Once DRIE has been completed, the electron resist is removed, resulting in the 1-D photonic crystal (Figure 20(d)). A diagram displaying the e-beam lithography/DRIE process for the patterning of PhC features has been provided in Appendix C.

7.2.3 Production of Microfluidic Channels

While the PhC is fabricated on the glass substrate, the microfluidic subsystem for cell focusing is fabricated separately. These microfluidic channels can be fabricated from polydimethylsiloxane (PDMS), an inert non-toxic polymer commonly used in the production of microfluidic devices. First, a mold must be produced to provide the structures for the microfluidic channels. The mold may be created by spin coating a 10 μm thick layer of SU-8 photoresist on a

silicon wafer, followed by patterning inversed features of a mold for microfluidic channels (20 μm wide). Liquid PDMS is then thoroughly mixed with a curing agent (10:1 volumetric ratio) and bubbles are removed using pressure swing in a vacuum chamber. Once the PDMS solution is prepared, it is then applied to the SU-8 mold and allowed to cure at 80◦C for 2.5 hours [50]. With the PDMS cured, it can then be gently removed from the mold, taking care not to damage the structures.

The PDMS must then be bonded to the PhC. As the silicon nitride PhC is only 1 μm wide, and the silicon dioxide substrate is exposed over the majority of the area, an oxygen plasma bonding treatment can be used to permanently attach the PDMS to the glass substrate. Before bonding, the PDMS and PhC must be cleaned by using isopropyl alcohol, DI water and then dried with nitrogen. Next, the PDMS and the PhC are placed in a reactive ion etching system (RIE) chamber with the surfaces to bond facing up [51]. The surfaces are then exposed to oxygen plasma for approximately 1 minute, after which the PDMS may be applied to the PhC [51]. The PDMS must be aligned with the PhC using a microscope, and possibly a micromanipulator, before it is pressed to the PhC, creating an irreversible bond.

7.3 Photonic Crystal Cell Scanning Probe

Lastly, one of the potential applications that we envision is single cell characterization using photonic crystals that can be performed without the need of microfluidics or a micro-flow cytometer device. Models have shown that as cells pass over the surface of the PhC, information regarding the cell can be obtained, including a 2-dimensional projection of the cell along its central cross section. Likewise, the same findings would apply if it is the PhC that passes over the surface of cells, rather than the former. And instead of a single line of cells, as simulated in flow cytometry,

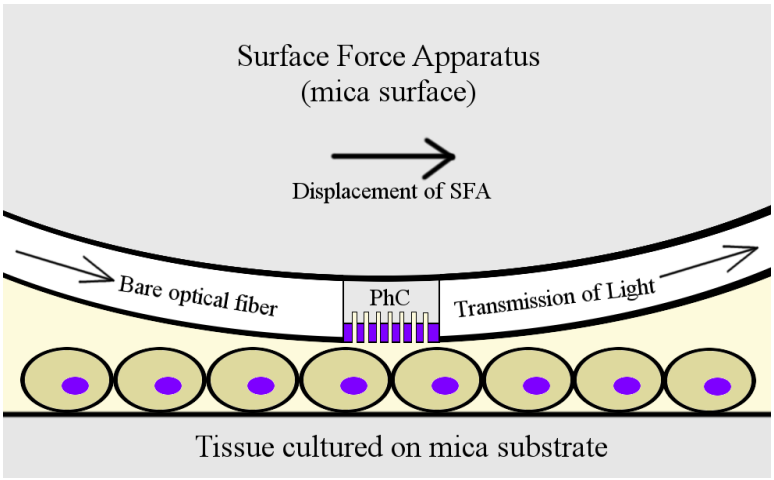

Figure 21. One potential design for a Photonic Crystal cell scanner shown on the curved mica cylinder of an SFA.

we could potentially study several lines, forming a layer of cells or a surface of a tissue. In Figure 21, a potential design for such a device is shown by incorporating a curved mica cylinder from a Surface Force Apparatus (SFA). The SFA is a device already widely used to characterize forces in colloids, however the design of its curved cylinders could possibly be suitable for mounting the PhC at its apex, and attaching bare optical fibers along the mica surface to convey light to and from the PhC. The PhC probe would scan a tissue, line by line in a manner similar to Atomic Force Microscopy (AFM), while recording the spectrum of the PhC probe. Each line scanned can be used to create a two dimensional projection of the cells in that line, and once each incremental line is scanned a three dimensional projection of the tissue can be created using topographical software.

CHAPTER 8

CONCLUSIONS

8.1 Note to Reader

Portions of this chapter have been adapted from work that has been previously published in *Optics Express,* 2014, 22, 12853-12860, and has been reproduced with permission from the Optical Society of America.

8.2 Conclusions

A novel design for a micro-flow cytometer using 1-D photonic crystals has been demonstrated. The device was modeled using finite difference time domain (FDTD) simulations. It was shown that the device is capable of not only detecting and counting cells, but is also able to provide information regarding cell shape, as well as its size. Furthermore if the refractive index of a cell is unknown, or likely to vary from cell to cell, by using the theorem of central moments we have been able to independently determine properties of cells such as diameter as well as their refractive index. Additionally, different wavelengths can be simultaneously used for multiple information channels. Altogether, this photonic crystal micro-flow cytometry system achieves several functions similar to the functions of large scale, traditional flow cytometry units, however on a scale small enough that the device may be integrated onto a chip. And by analyzing transmission density functions from a statistical approach, it should be very simple to program

such equations into computer software, allowing for a more sophisticated and precise method of analyzing cells, biological objects, and other complex micro particles.

REFERENCES

[1] O. Laerum, and T. Farsund, "Clinical Application of Flow Cytometry: a Review," Cytometry 2, 1-13 (1981).

[2] P. Mullaney, and J. Jett, "Flow Cytometry: An Overview," Lasers Biol. Med. 34, 179-193 (1980).

[3] R. Chang, "Flow cytometry's new scalability," BioOptics World, (2008). http://www.bioopticsworld.com/articles/print/volume-1/issue-4/features/feature-focus/flow-cytometryrsquos-new-scalability.html

[4] M. May, "Optical Diagnostics/Flow Cytometry: Advances in optical biodetection," BioOptics World, (2013). http://www.bioopticsworld.com/articles/print/volume-6/issue-1/features/advances-in-optical-biodetection.html

[5] S. Seo, T. Su, D. Tseng, A. Erlinger, and A. Ozcan, "Lensfree holographic imaging for on-chip cytometry and diagnostics," Lab Chip 9, 777-787 (2009).

[6] D. Ateya, J. Erickson, P. Howell, L. Hilliard, J. Golden, and F. Ligler, "The good, the bad, and the tiny: a review of microflow cytometry," Anal. Bioanal. Chem. 391, 1485-1498 (2008).

[7] S. Yang, K. Lien, K. Huang, H. Lei, and G. Lee, "Micro flow cytometry utilizing a magnetic bead-based immunoassay for rapid virus detection," Biosens. Bioelectron. 24, 855-862 (2008).

[8] H. Huang, T. Ger, Y. Lin, and Z. Wei, "Single cell detection using a magnetic zigzag nanowire biosensor," Lab Chip 13, 3098-3104 (2013).

[9] T. Ger, H. Huang, C. Huang, and M. Lai, "Single cell detection using 3D magnetic rolled-up structures," Lab Chip 13, 4225-4230 (2013).

[10] S. Hur, H. Tse, and D. Di Carlo, "Sheathless inertial cell ordering for extreme throughput flow cytometry," Lab Chip 10, 274-280 (2010).

[11] G. Lee, C. Lin, and G. Chang, "Micro flow cytometers with buried SU-8/SOG optical waveguides," Sens. Actuators, A 103, 165-170 (2003).

[12] H. Majaron, "Structural Coloration," presented at the Seminar for the Department of Mathematics and Physics (University of Ljubljana), Ljubljana, December 2013.

[13] K. Saitoh, and M. Koshiba, "Chromatic dispersion control in photonic crystal fibers: application to ultra-flattened dispersion," Opt. Express 11, 843-852 (2003).

[14] J. Joannopulos, P. Villeneuve, and S. Fan, "Photonic Crystals: putting a new twist on light," Nature 386, 143-149 (1997).

[15] A. L. Pyayt, D. A. Fattal, Zh. Li, and R. G. Beausoleil, "Nanoengineered optical resonance sensor for composite material refractive-index measurements", Appl. Optics 48 (14), 2613-2618 (2009).

[16] H. Sun, A. Pyajt, J. Luo, Z. Shi, S. Hau, A. Jen, L. Dalton, and A. Chen, "Broadband electric field sensor with electro-optic polymer micro-ring resonator on side polished optical fiber," in Photonics West, Proc. SPIE Vol. 6117, Second-Order NLO Materials and Applications II (2006).

[17] A. Pyajt, X. Zhang, J. Luo, A. Jen, L. Dalton, and A. Chen, "Optical micro-resonator chemical sensor," Proc. SPIE, V. 6556, P.65561D 1-6 (2007).

[18] A. Pyajt, J.Zhou, A. Chen, J. Luo, A. Jen, and L. Dalton, "Electro-optic polymer microring resonators made by photobleaching," in Photonics West, Proc. SPIE Vol. 6470, Organic Photonic Materials and Devices IX (2007).

[19] D. Fattal, M. Sigalas, A. L. Pyajt, Zh. Li, and R. G. Beausoleil, "Guided-mode resonance sensor with extended spatial sensitivity," Proc. SPIE 6640, 66400M 1-11 (2007)

[20] D. DiCarlo, D. Irimia, R. G Tompkins, and M. Toner, "Continuous inertial focusing, ordering and separation of particles in microchannels," PNAS 104, 18892-18897 (2007).

[21] S. Choi, and J. Park, "Continuous hydrophoretic separation and sizing of microparticles using slanted obstacles in microchanel," Lab Chip 7, 890-897 (2007).

[22] P. Howell, J. Golden, L. Hilliard, J. Erickson, D. Mott, and F. Ligler, "Two simple and rugged designs for creating microfluidic sheath flow," Lab Chip 8, 1097-1103 (2008).

[23] J. Shi, X. Mao, D. Ahmed, A. Colletti, and T. Huang, "Focusing microparticles in a microfluidic channel with standing surface acoustic waves (SSAW)," Lab Chip 8, 221-223 (2008).

[24] G. Segre, and A. Silberberg, "Radial particle displacements in Poiseuille flow of suspensions," Nature 189, 209-210 (1961).

[25] D. DiCarlo, J. Edd, K. Humphry, H. Stone, and M. Toner, "Particle Segregation and Dynamics in Confined Flows," Phys. Rev. Lett. 102, 094503 1-4 (2009).

[26] A. Chung, D. Gossett, and D. Di Carlo, "Three dimensional, Sheathless, and High-Throughput Microparticle Inertial Focusing through Geometry Induced Secondary Flows, Small 9, 685-690 (2013).

[27] H. Shapiro, *Practical Flow Cytometry* (Academic, 2005)

[28] N. Watkins, B, Venkatesan, M. Toner, W. Rodriguez, and R. Bashir, "A robust electrical microcytometer with 3-dimensional hydrofocusing," Lab Chip 9, 3177-3184 (2009).

[29] R. Horvath, "Finite Difference Solution of Maxwells Equations," in *Application of Numerical Analysis in Computational Science,* (Academic, 2004) pp. 1-10.

[30] Optiwave, "FDTD Basics" in *OptiFDTD Technical Background and Tutorials*, (Academic, 2008) pp. 3-8.

[31] K. Yee, "Numerical Solution of Initial Boundary Value Problems Involving Maxwell's Equations in Isotropic Media," IEE. Conf. Publ. 14, 302-307 (1966).

[32] X. Xuan, J. Zhu, and C. Church, "Particle focusing in microfluidic devices," Microfluid. Nanofluid. 9, 1-16 (2010).

[33] http://optiwave.com/category/products/component-design/optifdtd/

[34] T. Baak, "Silicon oxynitride; a material for GRIN optics," App. Opt. 21, 1069-1072 (1982).

[35] G. Gosh, "Dispersion-equation coefficients for the refractive index and birefringence of calcite and quartz crystals," Opt. Commun. 163, 95-102 (1999).

[36] S. Rahong, B. Saekow, S. Porntheerapat, J. Nukeaw, C. Hruanun, and A. Poyai, "Modification of the optical properties of polydimethylsiloxane (PDMS) for photonic crystal biosensor application," in *International Nanoelectronics Conference (INEC),* (IEEE, 2010).

[37] Y. Jin, J. Chen, L. Xu, and P. Wang, "Refractive index measurement for biomaterial samples by total internal reflection," Phys. Med. Biol. 51, N371-N379 (2006).

[38] T. Gregory, "The Bigger the C-Value, the Larger the Cell: Genome Size and Red Blood Cell Size in Vertebrates," Blood Cells, Molecules, and Diseases 27, 830-843 (2001).

[39] W. Jin, Y, Wang, N, Ren, M. Bu, X. Shang, Y. Xu, and Y. Chen, "Simulation of simultaneous measurement for red blood cell thickness and refractive index," Opt. Lasers Eng. 50, 154-158 (2012).

[40] B. Rappaz, A. Barbul, F. Charriere, J. Kuhn, P. Marquet, R. Korenstein, C. Depeursinge, and P. Magistretti, "Erythrocytes volume and refractive index measurement with a Digital Holographic Microscope," Proc. SPIE V. 6445, Optical Diagonostics and Sensing VII (2007).

[41] V. Maltsev, A. Hoekstra, and M. Yurkin, "Optics of White Blood Cells: Optical Models, Simulations, and Experiments," in *Advanced Optical Flow Cytometry: Methods and Disease Diagnoses*, (Academic, 2011), pp. 63-93.

[42] J. Stewart and A. Pyayt, "Photonic crystal based microscale flow cytometry," Opt. Express. 22, 12853-12860 (2014).

[43] H. Fogler, *Elements of Chemical Reaction Engineering, 4th ed* (Academic, 2006).

[44] A. Bagatur'yants, K. Novoselov, A. Safonov, V. Cole, M. Stoker and A. Korkin, "Silicon nitride chemical vapor deposition from dichlorosilane and ammonia: theoretical study of surface structures and reaction mechanism," Surf. Sci. 486, 213-225 (2001).

[45] R. Curley, T. McCormack, and M. Phipps, "Low-ressure CVD and Plasma-Enhanced CVD," http://www.ece.umd.edu/class/enee416/GroupActivities/LPCVD-PECVD.pdf.

[46] M. Ivanda, "Implementation and Development of the LPCVD Process," http://www.irb.hr/en/str/zfm/labs/lmf/Previous_projects/LPCVD/

[47] H. Albers, L. Hilderink, E. Szilagyi, F. Paszti, P. Lambeck and T. Popma, "Reduction of hydrogen induced losses in PECVD-SiOxNy optical waveguides in the near infrared," Lasers and Electro-Optics Society Annual Meeting Vol. 1, 88-89 (1995).

[48] https://www.memsnet.org/mems/processes/etch.html

[49] M. McCord, *SPIE Handbook of Microlithography, Micromachining and Microfabrication Vol. 1* (Academic, 2000)

[50] F. Burgoyne, "Rapid curing of PDMS for microfluidic applications," http://blogs.rsc.org/chipsandtips/2006/10/23/rapid-curing-of-pdms-for-microfluidic-applications/

[51] L. Xiong, P. Chen, and Q. Zhou, "Adhesion promotion between PDMS and glass by oxygen plasma pre-treatment," J. Adhes. Sci. Technol. 28, 1046-1054 (2014).

APPENDIX A

COPYRIGHT PERMISSIONS

The following document expresses permission from the Optical Society of America to reproduce content from our previously published content. This applies to chapters 1, 4, 5, 6 and 8.

Justin Stewart <jwstewar@mail.usf.edu>

Permission to use article in thesis

pubscopyright <copyright@osa.org> Wed, Aug 20, 2014 at 5:24 PM
To: Justin Stewart <jwstewar@mail.usf.edu>

Dear Mr. Stewart,

Thank you for contacting The Optical Society.

Because you are the author of the source paper from which you wish to reproduce material, OSA considers your requested use of its copyrighted materials to be permissible within the author rights granted in the Copyright Transfer Agreement submitted by the requester on acceptance for publication of his/her manuscript. It is requested that a complete citation of the original material be included in any publication. This permission assumes that the material was not reproduced from another source when published in the original publication.

Please let me know if you have any questions.

Kind Regards,

Susannah Lehman

Susannah Lehman

August 20, 2014

Authorized Agent, The Optical Society

APPENDIX B

DESCRETIZED MAXWELLS EQUATIONS FOR TM POLARIZATION

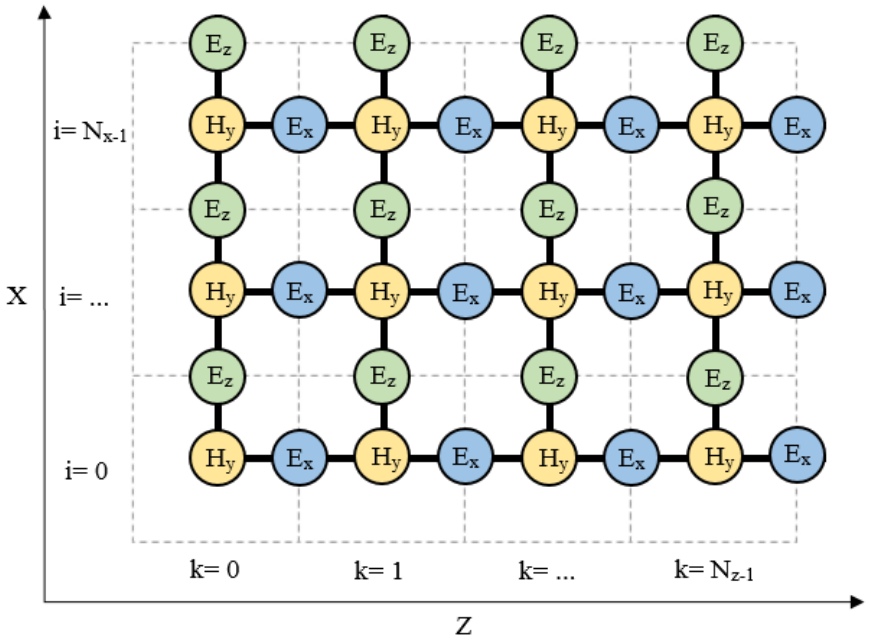

Figure A. Location of the electric and magnetic fields within the computational domain for TM polarization.

$$H_y^n(i,k) = H_y^{n-1}(i,k) + \frac{\Delta t}{\mu}\left[\frac{E_x^{n-1/2}(i,k+1/2) - E_x^{n-1/2}(i,k-1/2)}{\Delta Z}\right]$$

$$-\frac{\Delta t}{\mu}\left[\frac{E_z^{n-1/2}(i+1/2,k) - E_z^{n-1/2}(i+1/2,k)}{\Delta X}\right]$$

$$E_x^{n+1/2}(i,k+1/2) = E_x^{n-1/2}(i,k+1/2) + \frac{\Delta t}{\varepsilon}\left[\frac{H_y^n(i,k+1) - H_y^n(i,k)}{\Delta Z}\right]$$

$$E_z^{n+1/2}(i+1/2,k) = E_z^{n-1/2}(i+1/2,k) - \frac{\Delta t}{\varepsilon}\left[\frac{H_y^n(i+1,k) - H_y^n(i,k)}{\Delta X}\right]$$

APPENDIX C

PHC LITHOGRAPHY AND ETCHING PROCESS FLOW DIAGRAM

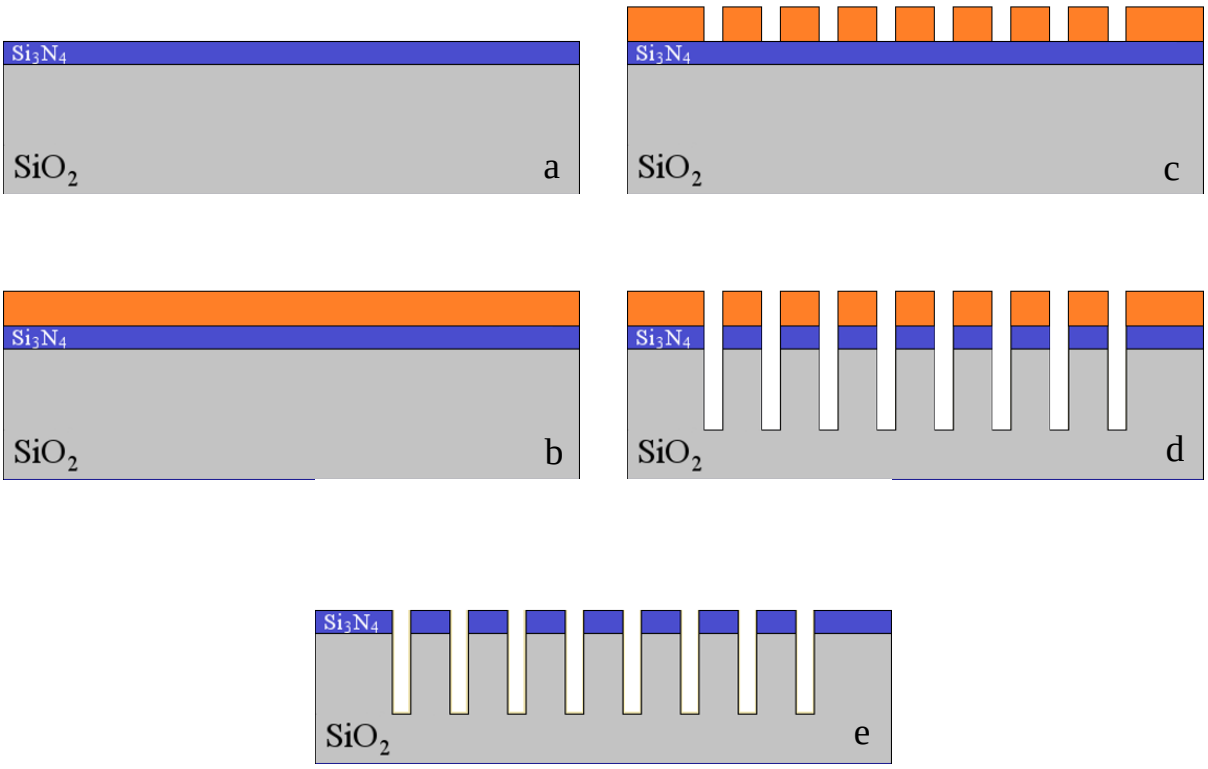

Figure B. Fabrication steps for the patterning of PhC features. (a) The silicon nitride waveguide is coated with an electron sensitive resist (b). After exposure to an electron beam and rinsing with a developer, the pattern is transferred to the resist (c). Next DRIE is used to etch through the nitride and silicon dioxide layers (d). Finally the resist is removed leaving behind the PhC (e)